Novel eco-friendly Mg-Zn-Ca-Mn nanocomposite for water treatment and environmentally remediation of textile and pharmaceutical industries effluents

S. Sankaralinga Raja[1*], M. Sivapragash[2], R. Rajesh[3] and K. Hari Ram[4]

[1]Department of Mechanical Engineering, Sree Vaikundar Polytechnic College, Pillayarpuram, Kanyakumari District, Tamil Nadu, India.
[2]Department of Mechanical Engineering, Narayanaguru College of Engineering, Manjalumoodu, Kanyakumari District, Tamil Nadu, India.
[3]Department of Mechanical Engineering, Rohini College of Engineering & Technology, Palkulam, Kanyakumari District, Tamil Nadu, India.
[4]Department of Mechanical Engineering, DMI Engineering College, Aralvaimozhi, Kanyakumari District, Tamil Nadu, India.
*to whom all correspondence should be addressed: sankaralingarajas@gmail.com

Abstract

The current work elucidates the significance of nanometal oxide composites for enhanced environmental remediation applications. An efficient photocatalyst has been prepared by synthesising a multi-metal oxide nanocomposite that combines MgO, ZnO, CaO, and MnO2 nanoparticles during the synthesis process. The nanocomposite was prepared using a simple sol-gel method, where each precursor was mixed with NaOH as a reducing agent. XRD analysis confirms the high purity and crystallinity of the composite, revealing a cubic MgO and CaO phase alongside hexagonal ZnO and MnO_2 phases, with a calculated crystallite size of 19.74 nm. FESEM analysis reveals a rod-like MgO structure surrounded by agglomerated spherical ZnO, CaO, and MnO_2 particles, indicating strong surface charge interactions. EDX confirms the successful formation of a pure nanocomposite. UV-Vis spectroscopy confirmed distinct absorption peaks at 226 nm (MgO), 273 nm (MnO_2), 313 nm (CaO), and 382 nm (ZnO), indicative of the coexistence of multiple oxides within a single matrix. The results confirm the formation of Mg-Zn-Ca-Mn nanocomposite with excellent physico-chemical properties. Additionally, the nanocomposite demonstrates excellent antioxidant activity, stabilising DPPH radicals with a maximum scavenging efficiency of 96.14 % at 800 µg/mL. Under sunlight irradiation, it achieves 99.68% degradation of Rhodamine B in 60 minutes and 98.55% degradation of Amlodipine in 90 minutes, following pseudo-first-order kinetics. Reusability tests confirm the structural and functional stability of the material over five cycles, reducing degradation efficiency by only 4.1% for Rhodamine B and 5.3% for Amlodipine. The characterisations and observations indicated that the prepared nanocomposite can be an excellent source for environmental remediation applications.

Keywords: Antimicrobial performance, Environmental remediation, Pharmaceutical industries, Photocatalytic activity, Textile industries.

1. Introduction

The scientific community has shown significant interest in nanoscale materials, which typically range in size from 1 to 100 nanometers (nm). These materials have garnered attention due to their distinct properties, which vary from those of bulk materials. Researchers are particularly intrigued by the potential applications of nanoscale materials in various fields, such as nanoelectronics, nanocatalysis, and nanomedicine (Chen *et al.,* 2016). Moreover, synthesising nanocomposites involves mixing multiple distinct materials to achieve the desirable properties of the individual fundamental materials. Both essential materials influence the properties of an NC, as well as their morphology and interfacial features. The versatility of nanocomposites arises from their distinctive structural, thermal, and optical properties, which enable them to exhibit enhanced performance across a wide range of technological applications. The remarkable impact of metal NCs has been discovered in numerous findings owing to their notable features, such as a high surface area, high porosity, low cost, long lifetime, thermal stability, and the ability to tune their composition and morphology (Dontsova *et al.,* 2019). The material's high performance in various fields can be attributed to its novel physical and chemical properties, which result from the combination of two or more metal oxides.

Water is a vital resource for all life on Earth, playing a crucial role in ecosystems, human health, and industry (Gavrilescu, 2021; Tabet et al., 2024). It covers approximately 71% of the Earth's surface, with the vast majority of this area located in the oceans. However, only about 2s.5% of Earth's water is freshwater, essential for drinking, agriculture, and sanitation. The elimination of pollutants from pharmaceutical and textile industries into water bodies is a critical environmental issue due to the persistence and toxicity of these contaminants (Rathi *et al.,* 2021; Raveena & Surendran, 2024; Venkatraman & Surendran, 2023). Pharmaceuticals, including antibiotics, hormones, and painkillers, can enter water bodies through improper disposal, wastewater treatment plant effluents, and agricultural runoff. Similarly, textile pollutants, including dyes, heavy metals, and synthetic chemicals, can be released from industrial wastewater during textile manufacturing (Kir et al., 2024; Uddin, 2021). Removing pharmaceutical and textile pollutants from water bodies often requires a combination of physical, chemical, and biological methods. Advanced oxidation processes, adsorption, membrane filtration, bioremediation, electrochemical treatments, and coagulation/flocculation are all effective strategies.

The discharge of Amlodipine, a pharmaceutical drug, and Rhodamine B, a synthetic dye, from industries poses significant environmental risks due to their toxicity and persistence in water bodies (Khan *et al.,* 2023). Amlodipine, often released from pharmaceutical manufacturing and hospital effluents, can disrupt aquatic ecosystems and resist conventional wastewater treatment. Amlodipine is designed to be biologically active, so its release into the environment can disrupt marine ecosystems. Even at low concentrations, Amlodipine can affect the growth, reproduction, and behaviour of aquatic organisms and may contribute to the development of antibiotic resistance. Rhodamine B, used in textiles and dye manufacturing, is also utilised as an artificial food colourant and is toxic to aquatic life, causing visual disruption (Dave et al., 2022; Legmairi et al., 2023). Additionally, it is a carcinogenic and mutagenic substance, posing potential risks to human health if it contaminates drinking water supplies. These two pollutants are taken as a model effluent for the degradation of textile and pharmaceutical effluents. In addition to the discharge of pollutants from textiles and pharmaceutical industrial wastes, water pollution can also occur due to various microorganisms, including fungi, bacteria, viruses, and other similar agents. It has been well-established in the scientific literature that the presence of bacteria in drinking water is associated with severe diseases, including typhoid, cholera, and bacillary dysentery (Gong *et al.*, 2023). The emergence of multidrug-resistant (MDR) strains is increasingly recognised as a significant challenge, primarily attributed to their ability to develop resistance against conventional synthetic water disinfectants. Therefore, there is an urgent need for multifunctional nanomaterials capable of addressing organic pollutants, microbial contamination, and regulating reactive oxidative species (ROS) in a single, integrated system (Goodarzi *et al.,* 2024; Kamani *et al.,* 2024; Moein *et al.,* 2025).

Adding multiple metal oxides to a composite enables the combination of different properties to achieve enhanced performance tailored to specific applications (Abdipour & Hemati, 2024; Delavari *et al.,* 2024; Jonidi Jafari *et al.,* 2024; Mourdikoudis *et al.,* 2021; Rajabizadeh *et al.,* 2025). Each metal oxide contributes unique characteristics, such as improved temperature stability, mechanical strength, chemical inertia, and electrical conductivity. Notably, we have reviewed several metal oxide nanoparticles for their feasibility, economic viability, potential ability, and biocompatibility as photocatalysts (Abdipour et al., 2024; Asgari et al., 2024; "Elimination of nickel and chromium(VI) ions from industrial wastewater by electrodialysis/characteristics/impact of parameters," 2024; Khalooei et al., 2024; Qi et al., 2017; Zeghdi et al., 2024). Upon considering various metal oxides based on the criteria mentioned above, the present study aims to develop and characterise a multifunctional Mg-Zn-Ca-Mn nanocomposite using a cost-effective sol-gel method for environmental remediation. The nanocomposite contains catalytically active sites (e.g., metal oxide domains) capable of generating reactive oxygen species (ROS) under light or in the presence of oxidants. ZnO and MgO nanoparticles exhibit promising antimicrobial properties. Multiple studies have demonstrated the effectiveness of ZnO and MgO nanoparticles in suppressing the proliferation of Escherichia coli, a bacterium commonly present in urban wastewater, as well as Staphylococcus aureus and certain multidrug-resistant strains (Sharma *et al.,* 2023). CaO contributes by creating a highly alkaline environment that inhibits microbial growth and supports pollutant degradation (Gharbi et al., 2024; Yang et al., 2021). MnO enhances photocatalytic efficiency through improved electron transfer and redox reactions, thereby facilitating pollutant breakdown and bacterial inhibition (Khan *et al.,* 2023). Together, these oxides create a powerful multifunctional composite for water cleansing and decontamination applications. The motivation behind this study stems from the increasing need for eco-friendly, scalable solutions to combat industrial wastewater pollution and microbial contamination. The integration of multiple metal oxides (MgO, ZnO, CaO, and MnO_2) into a single composite enhances synergistic charge transfer and electron-hole separation, thereby improving photocatalytic activity beyond that of individual metal oxide systems. This work bridges existing gaps by developing a multifunctional nanocomposite capable of simultaneously addressing pollutant breakdown, bacterial inhibition, and radical stabilisation (Feng *et al.,* 2024; Xu *et al.,* 2025). Moreover, the scope of the study encompasses water treatment applications, with a focus on the degradation of pharmaceutical and textile effluents. Antimicrobial activity assessments, targeting waterborne bacterial contaminants and antioxidant analysis, validate the nanocomposite's ability to regulate ROS balance.

This study presents a novel Mg-Zn-Ca-Mn nanocomposite synthesised via a simple sol-gel method, integrating four distinct metal oxides to achieve multifunctional environmental remediation capabilities (Meneceur et al., 2025; Salmi, Zelca, et al., 2024). Unlike previously reported nanomaterials, this work uniquely combines MgO, ZnO, CaO, and MnO_2, enhancing photocatalytic degradation, antibacterial performance, and antioxidant activity simultaneously. The prepared nanocomposite is analysed for its functional, optical, structural, and morphological properties. The efficiency of the prepared nanocomposite in treating industrial effluents, such as Rhodamine B and Amlodipine, was recorded under sunlight. The nanocomposite exhibits remarkable photocatalytic efficiency, achieving 99.68% degradation of Rhodamine B in 60 minutes and 98.55% degradation of Amlodipine in 90 minutes, outperforming conventional metal oxide composites. The antimicrobial performance of prepared Mg-Zn-Ca-Mn NC against *E. coli*, *S. aureus*, and DPPH was evaluated with varied concentrations. The activity of the prepared nanocomposite towards industrial effluents and microbes was studied, and its mechanism is proposed below.

2. Materials and methods

Magnesium acetate tetrahydrate (Mg $(CH_3COO)_2 \bullet 4H_2O$) (Purity 98.5%), Zinc acetate dihydrate Zn $(CH_3CO_2)_2 \cdot 2H_2O$ (Purity 99.5%), Calcium acetate (Ca $(CH_3CO_2)_2$) (Purity 99.0%), Manganese acetate (Mn (CH_3CO_2) $2 \cdot (H_2O)$) (Purity 99%), Sodium hydroxide pellets (NaOH) (Purity 97%), Ethanol (Purity 98%), Rhodamine B, Amlodipine. All were obtained from commercial sources, were analytical grade, and were used exactly as supplied. Throughout the trials, double-distilled water was used.

2.1. Preparation of Mg-Zn-Ca-Mn nanocomposite

About 0.1 M of Magnesium acetate, Zinc acetate, Calcium acetate, and Manganese acetate were individually dissolved in 50 ml of DD water with stirring assistance. The ratio was chosen to maximise the synergistic interaction between the components, ensuring that the strengths of each oxide complement the others and that there are equal contributions and active sites for each compound. The stirring continued until a homogeneous solution was formed. Subsequently, the individual solutions were carefully introduced into a magnesium acetate solution in a gradual and controlled manner, resulting in the development of a homogeneous mixture. To induce the formation of precipitates, a solution of NaOH was added dropwise to the precursor solution while stirring vigorously until the pH reached 10. The formation of brownish precipitates was observed to occur rapidly and without delay.

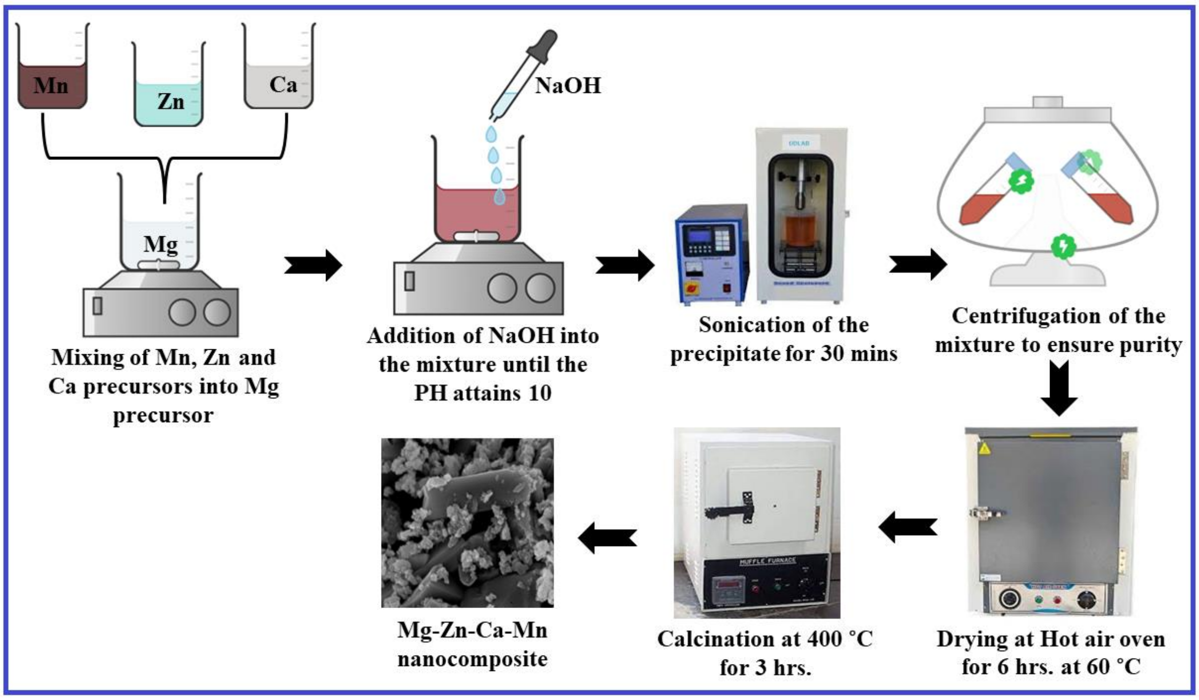

Figure 1. Preparation of Mg-Zn-Ca-Mn nanocomposite

The mixture was subjected to continuous stirring at ambient temperature for 4 hours. After stirring, the mixture undergoes sonication for 30 minutes to achieve a homogeneous dispersion of nanoparticles. The sonicated mixture is left undisturbed overnight to undergo the ageing process, allowing sufficient time for the desired reactions to occur. As a result, a precipitate forms and settles at the bottom of the beaker. The precipitates underwent several washes with DD water and were filtered using a centrifuge. The materials that underwent filtration were then dried at 60°C for 6 hours. Subsequently, an annealing process was carried out at 400°C for 3 hours. The synthesis procedure is schematically depicted in Figure 1.

2.2. Sample preparation for photocatalytic degradation

The photocatalytic performance against Rhodamine B and Amlodipine in the occurrence of the prepared nanocomposite under sunlight was estimated as follows. Rhodamine B and amlodipine pollutants at a concentration of 100 mg were mixed thoroughly in 100 mL of deionised water and stored as a stock solution. Then, 100 mg of the prepared nanocomposite is added separately to the pollutants. The nanoparticle-suspended pollutants were irradiated under sunlight for 60 minutes for Rhodamine B and 90 minutes for Amlodipine, respectively. A UV-vis spectroscopy examination was performed on the appropriate quantity of pollutants at intervals of 15 minutes. After that, the deterioration was assessed based on their degree of optical absorption, and the UV-vis spectrum was recorded regularly. Furthermore, the efficiency of pollutant degradation by the nanomaterials was demonstrated using equation (1) below. (Karthikeyan, *et al.,* 2023).

$$Degradation\ efficiency\ (\%)\ = \left(1 - \frac{Ct}{C0}\right) \times 100\ \% \tag{1}$$

Where, c_t and c_0 are the final and initial concentrations of the respective pollutants, to specifically evaluate the Reactive oxygen species (ROS) involved in the degradation process, the scavenging activity was performed with 5mM of various scavengers, including $AgNO_3$, isopropyl alcohol (IPA), acetic acid (AA), and p-benzoquinone (pBQ) for electron (e-), hydroxyl (.OH), hole (h^+) and superoxide ($O_2^{\cdot -}$) scavenging, respectively.

2.3. Preparation of MHA medium

Mueller-Hinton agar medium is prepared by measuring 1 litre of distilled water, adding 38 grams of Mueller-Hinton agar powder, and stirring to prevent clumping. Stir and warm gradually until the mixture is completely dissolved. To sterilise, autoclave at 121°C for 15 minutes. Once the mixture has cooled to 45–50°C, transfer it onto sterile Petri dishes, filling each to a depth of approximately 4 mm (25–30 ml). Allow the agar to firm at room temperature, then store the plates in a covered container at 4°C until needed. To avoid contamination, sterile procedures should be kept up at all times. Then, the agar medium was swabbed with bacteria using sterile earbuds, and holes were made using a micropipette needle. The holes were filled with varied loadings of NPs, such as 25, 50, and 100 mg/mL, and streptomycin was used as a standard. Then, the inhibited zone was measured after a 24-hour incubation period using a screw gauge.

2.4. Antioxidant assay

The 2,2-diphenyl-1-picrylhydrazyl (DPPH) approach was employed to calculate the ability of the prepared nanocomposite to neutralise free radicals using methanol as a solvent. First, 100 μL of a nanocomposite containing multiple loadings, such as 25, 50, and 100 mg/mL, was introduced to a test tube containing 2 mL of 0.1 mM DPPH, and the volume was then increased to 3 mL. Before analysing the wavelength at 517 nm, the reaction solution was kept at the ambient temperature for 40 min in the dark. The DPPH solution was chosen as a control by adding 1 mL of methanol. The following equation (2) calculates the DPPH scavenging activity (Barani et al., 2025; Locatelli et al., 2009), where CA and TA stand for control absorbance and test absorbance, respectively.

$$\text{Antioxidant activity} = \frac{CA - TA}{CA} X\,100\ \ \% \qquad (2)$$

2.5. Characterisation techniques

An analysis of the structural characteristics of the Mg-Zn-Ca-Mn nanocomposite was conducted using XRD. The molecular vibration and functional groups of Mg-Zn-Ca-Mn nanocomposite were recorded using FTIR. The analysis of the surface morphology of the Mg-Zn-Ca-Mn nanocomposite was conducted using FESEM. Additionally, EDX was utilised to reveal the elemental composition present in the materials. The optical absorbance level of the synthesised Mg-Zn-Ca-Mn nanocomposite was measured using a UV-Vis spectrophotometer. The luminescence properties of the prepared Mg-Zn-Ca-Mn nanocomposite were examined using photoluminescence spectroscopy. The spectroscopy was conducted using a Cary Eclipse instrument manufactured by Agilent Technologies in Singapore.

3. Result and discussion

3.1. Structural analysis

The structural phase and crystalline nature of the prepared nanocomposite were determined by XRD analysis, as depicted in Figure 2. The results show that many peaks arise from 2 theta, which confirms the presence of Mg, Zn, Ca, and Mn in the composite. The emerging peaks are 10.78, 29.42, 31.77, 34.43, 36.2, 39.39, 42.87, 47.53, 56.48, 62.75, 67.81, 69.08 and 77.01. From the observations, the MgO arises from 36.20, 42.87, 62.75, and 77.01, corresponding to Miller indices (111), (200), (220), and (222), respectively, and exhibits a cubic structural phase, as per JCPDS No. 45-0946 (Zahran *et al.,* 2018).

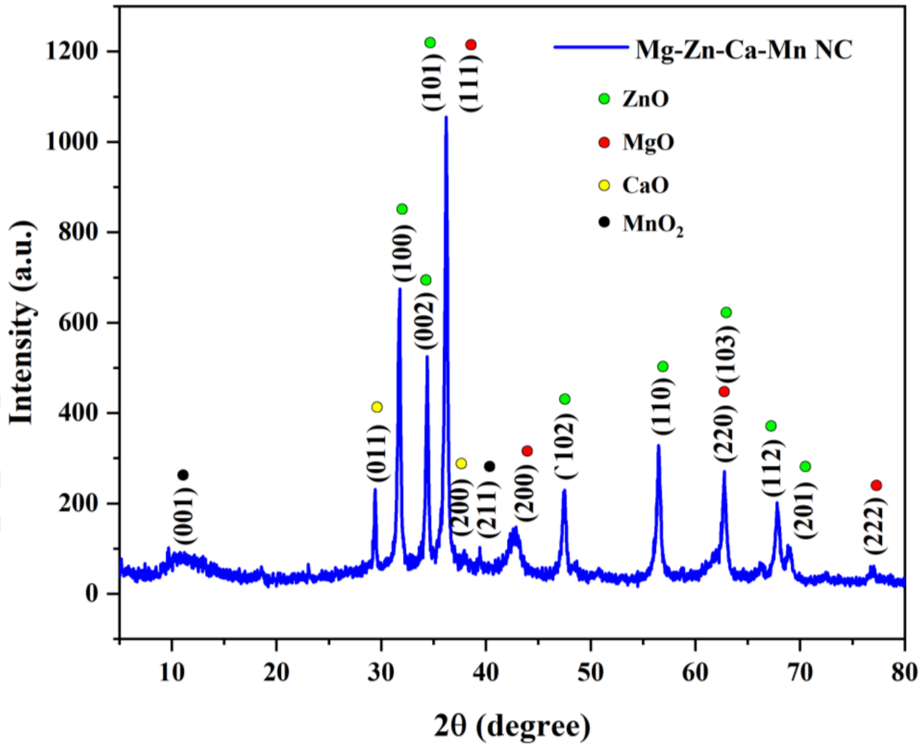

Figure 2. XRD analysis of the prepared Mg-Zn-Ca-Mn nanocomposite

The ZnO attributes to 31.77, 34.4, 36.2, 47.53, 56.48, 62.75, 67.81, and 69.08, which corresponds to (100), (002), (101), (102), (110), (103), (112) and (201) respectively that exhibits a hexagonal wurtzite ZnO phase that matches the JCPDS NO. 36-1451(Fang *et al.,* 2014). The MnO_2 reveals the hexagonal phase at positions 10.78 and 39.39, which correspond to the (001) and (211) planes (JCPDS Card No: 44-0141) (Zhu *et al.,* 2012). Finally, the CaO was confirmed to be present at 29.42 and 37.93, corresponding to the (011) and (200) planes, respectively (JCPDS Card No: 37-1497) (Xiao *et al.,* 2015). The crystal size of the prepared nanocomposite was found using the Debye-Scherrer equation (3) (Bokuniaeva & Vorokh, 2019).

$$D(crystallite\ size) = \frac{0.9\lambda}{\beta\ Cos\theta} \tag{3}$$

The crystal size of the nanocomposite is calculated to be 19.74 nm, which aligns with the FESEM and PSA results discussed below. The dislocation density of the nanocomposite is estimated to be 2.5 x 10^{-3} nm^{-2}. Typically, higher crystallinity is associated with lower dislocation density, and the low dislocation density observed here indicates the nanocomposite's excellent crystallinity. (Mu *et al.,* 2022). It is noted that XRD observations exhibit only the peaks of MgO, ZnO, CaO, and MnO_2, indicating the high purity of the prepared nanocomposite.

3.2. Morphological analysis

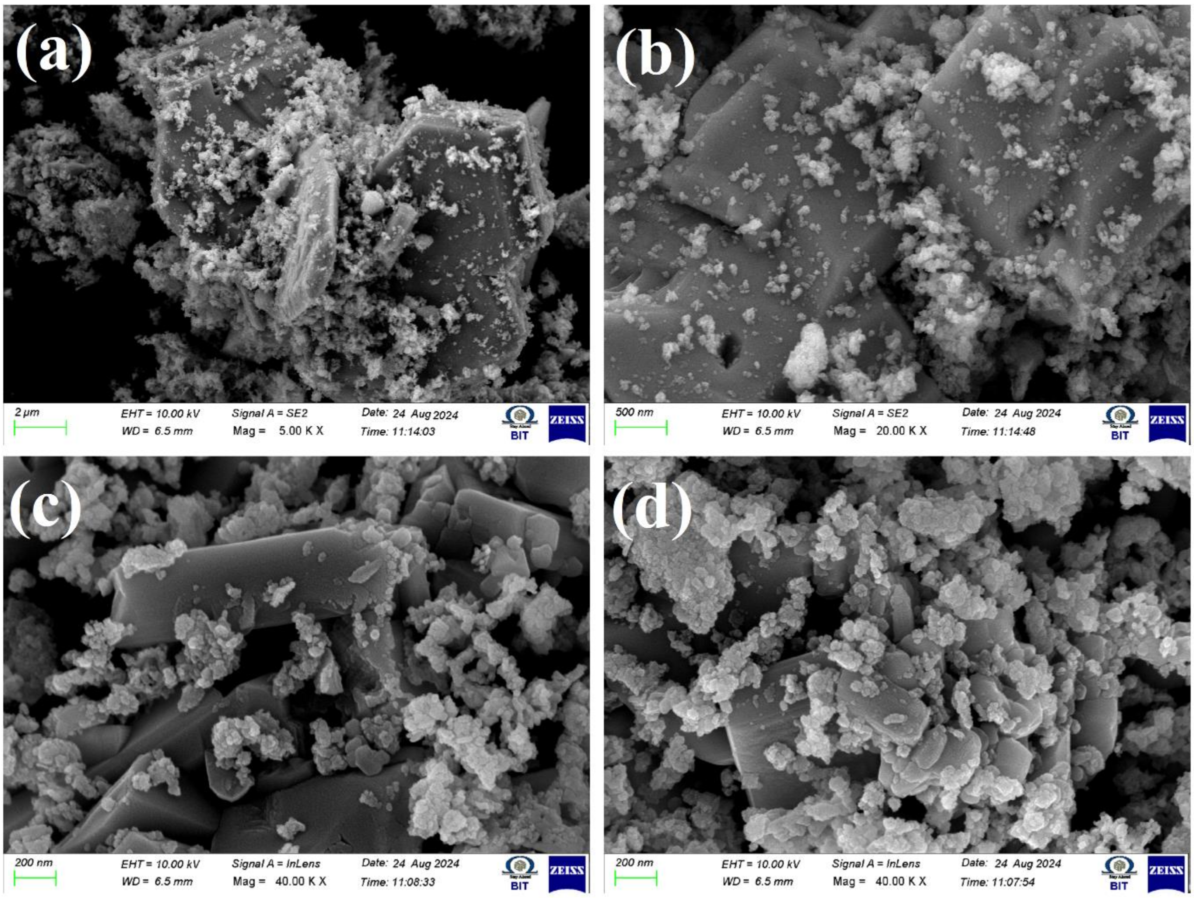

Figure 3. FESEM images of Mg-Zn-Ca-Mn nanocomposite

The surface morphology of the nanocomposite is revealed using FESEM, as depicted in Figure 3. The results suggest that the prepared nanocomposite exhibits a rod morphology with agglomerated spheres surrounding it.

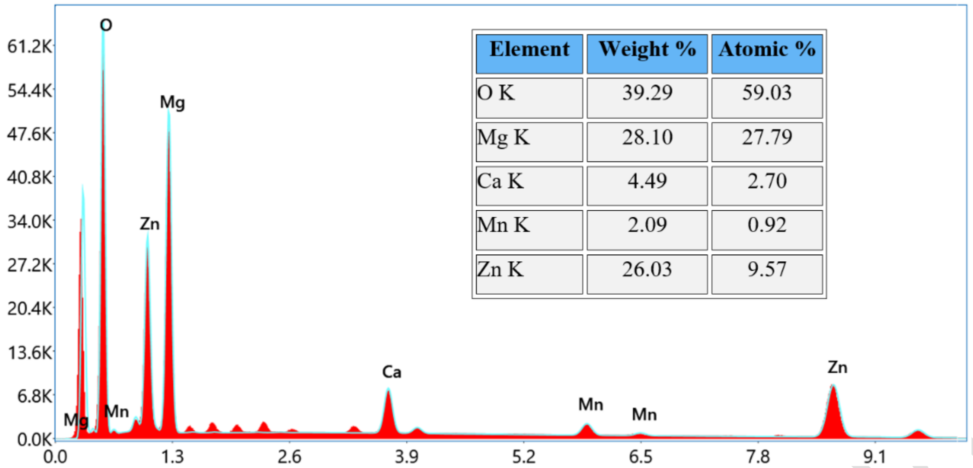

Element	Weight %	Atomic %
O K	39.29	59.03
Mg K	28.10	27.79
Ca K	4.49	2.70
Mn K	2.09	0.92
Zn K	26.03	9.57

Figure 4. EDX spectrum of Mg-Zn-Ca-Mn nanocomposite

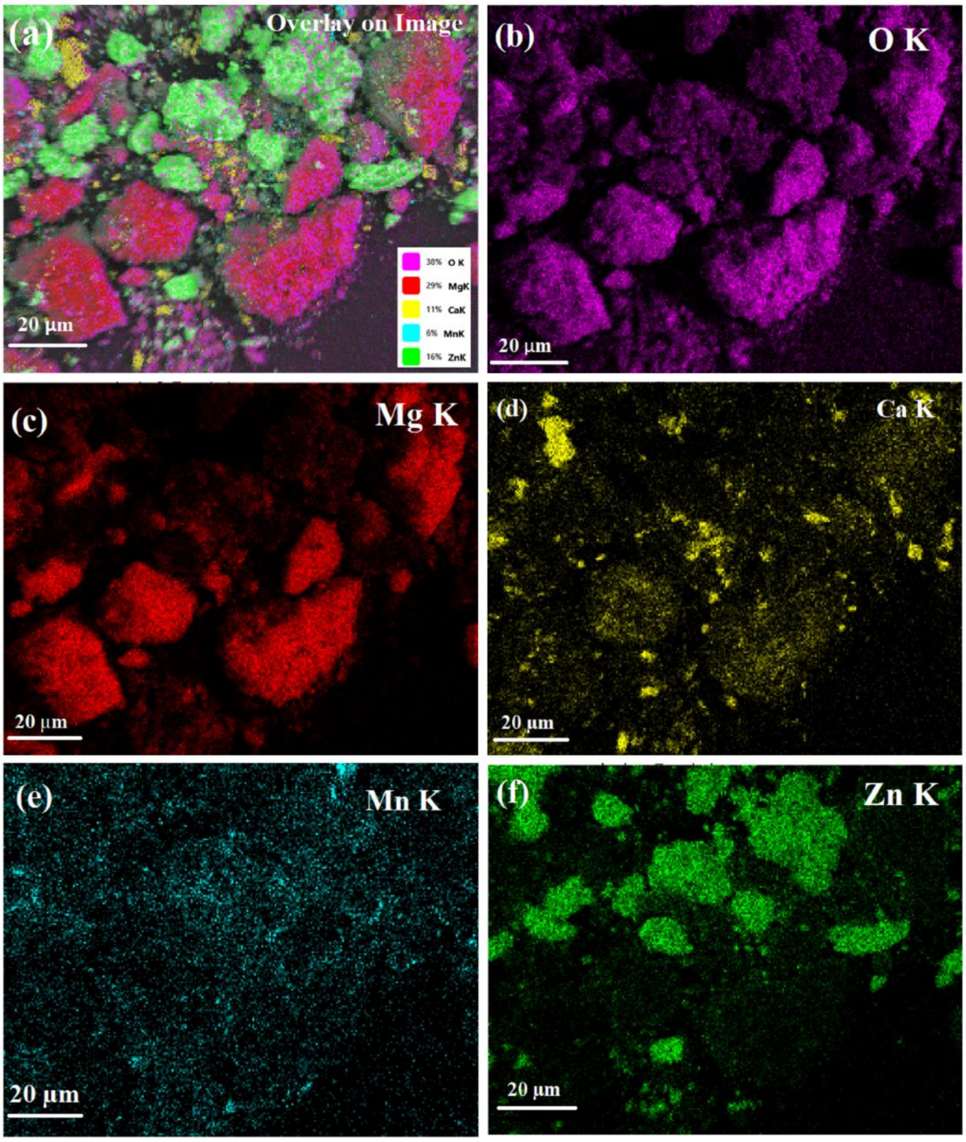

Figure 5. Elemental mapping for Mg-Zn-Ca-Mn nanocomposite

The formation of the rod may correspond to the Magnesium oxide NPs, as the XRD pattern matches the previous findings (Hassan *et al.,* 2021). The remaining elements, such as CaO, ZnO, and MnO_2, evolve as a sphere that surrounds the rod and are agglomerated in nature. The agglomeration and attraction of spheres towards the MgO rod are due to the composite's high surface charge of the prepared nanoparticles. The prepared spheres also match the XRD crystal size and particle size analysis findings. The EDAX mapping is analysed to find the overall elemental composition of the prepared nanocomposite, as seen in Figure 4. The analysis shows the composition occurrence of O, Mg, Zn, Ca, and Mn from the K shell. The availability of elements in the composite represents the successful formation of a pure Mg-Zn-Ca-Mn nanocomposite. The presence of MgO is higher than that of other elements, which aligns with the XRD results due to its rod-like structure. Elemental mapping was used to analyse the presence of various elements in a specific area. It shows the presence and position of Mg, Zn, Ca, Mn, and O elements in the overlay image, which confirms the formation of the nanocomposite shown in Figure 5. The presence of oxygen is higher, as indicated by both EDX and elemental mapping, resulting from the formation of an oxide bond with the metal elements in the composite. The result also suggests that Mg dominates in the composite due to the formation of rod morphology, as discussed in XRD, EDX, and FESEM images.

3.3. Functional group identification

The presence of various functional groups in the prepared nanocomposite has been confirmed through Fourier transform infrared spectroscopy, as shown in Figure 6. The observation shows that the nanocomposites possess various stretching vibrations at 3394, 2923, 2857, 1629, 1574, 1432, 1110, and 582 cm^{-1}. An intense stretching at 3394 cm^{-1} represents the occurrence of OH groups in the nanocomposite, which may occur during the preparation of KBr pellets for the analysis (Gautam *et al.,* 2016). The emergence of symmetrical vibration of the $=CH_2$ and $-CH_3$ groups, which suggests the availability of the alkanes, is responsible for the mild peak at 2923 cm^{-1} and 2857 cm^{-1}, respectively (Maravelaki-Kalaitzaki, 2005). The bands at 1629 cm^{-1} were attributed to the H–O–H bending mode, representing the deformation of water molecules adsorbed. The bands in the range of 1574 cm^{-1} are due to symmetric and asymmetric vibration of the C–O group. The prepared nanocomposite can absorb atmospheric carbon, as evidenced by the presence of a C-O group in the composite (Roy *et al.,* 2012). These bands, cited at 1432 cm^{-1}, originated from moisture and were assigned to the OH mode of adsorbed water. The weak band at 1110 cm^{-1} represents the presence of saturated alcohols (-OH) in the composite. The presence of various metal oxides exhibits the peaks at 1037, 680, 582, and 534 cm^{-1}, which represent Mn, Ca, Mg, and Zn metals, respectively, which confirms the formation of Mg-Zn-Ca-Mn nanocomposite (Al Sdran *et al.,* 2024; Pisu *et al.,* 2020; Srinivas *et al.,* 2021; Vodyanitskii, 2009).

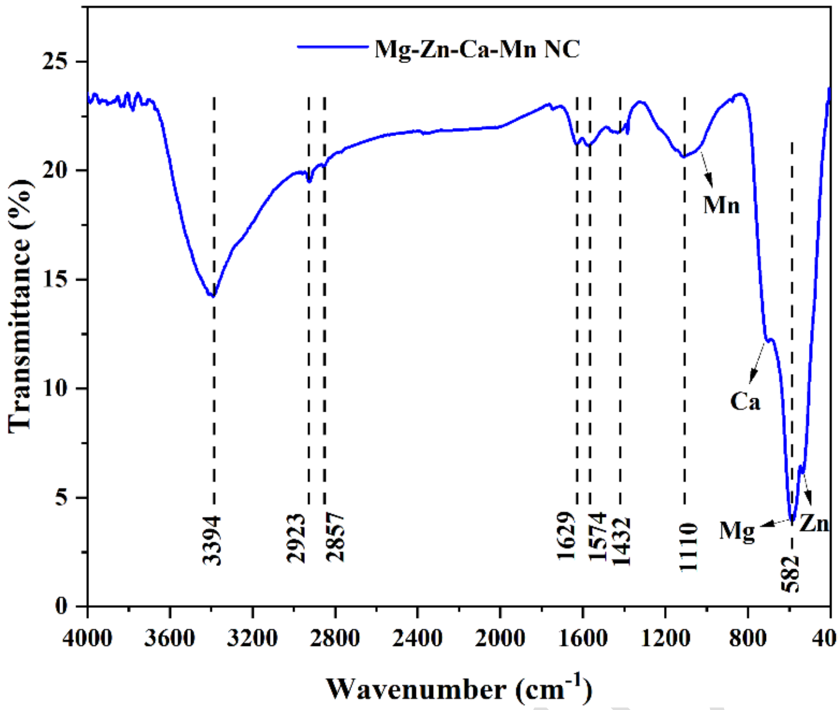

Figure 6. FTIR analysis of Mg-Zn-Ca-Mn nanocomposite

3.4. Particle size determination

The average particle size of NC was determined using the dynamic light scattering technique (Figure 7), in which the size of particles in the Brownian motion was calculated. The result implies that the average size of the prepared nanocomposite (d_{50}) is 36.64 nm.

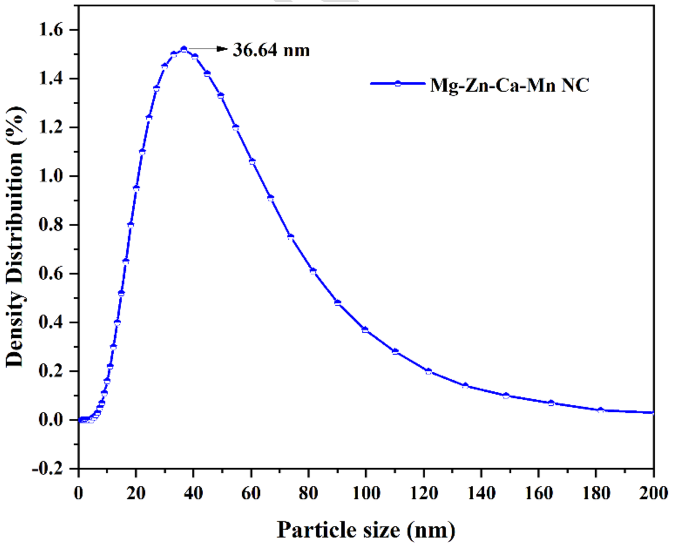

Figure 7. DLS analysis of prepared Mg-Zn-Ca-Mn nanocomposite

The d_{10} and d_{90} values of the prepared nanocomposite are 4.64 and 90.32 nm, respectively, indicating that the composite is present in the nanometre range. The broad peak observed in the result suggests that most of the particles in the prepared nanocomposite are available in a d50 range. The results also fit the previous SEM particle size and XRD crystalline size.

3.5. Optical properties

Optical absorption studies can determine the bandgap of metallic, non-metallic, and semiconductor materials. Figure 8(a) presents the UV spectra of the Mg-Zn-Ca-Mn nanocomposite, illustrating the wavelengths at which the material absorbs electromagnetic radiation. The observed absorption edges in the nanocomposite can be attributed to the scattering phenomenon arising from distinct oxide phases within the material. A broad spectrum was noticed at 226, 273, 313, and 382 nm, indicating four oxides coexist in a single matrix. The observation shows that the peak at 226 nm corresponds to MgO, 273 nm to MnO2, 313 nm to CaO, and 382 nm to ZnO absorptions. Within the absorption spectrum's long-wavelength region, the presence of a long tail is likely attributed to the scattering of radiation from mixed oxide clusters. The optical bandgap (Eg) can be evaluated using the fundamental absorption mentioned in equation (4). This involves determining the correlation between the incoming photon energy(hυ) and the absorption coefficient (α) (Santika *et al.,* 2024).

$$\alpha(\upsilon)h = K(hv - Eg)^n \tag{4}$$

The calculated Eg of the nanocomposite is 2.9 eV, as shown in Figure 8 (b). The region with the least energy difference between the top and bottom of the conduction and valence bands is known as the bandgap (Munawar *et al.,* 2020). The measured band gap of 2.9 eV for the prepared nanocomposite is notably smaller than that of the individual metal oxides reported in the literature, such as MgO (4.2-5.8 eV), ZnO (3.10-3.37 eV), CaO (3.0-4.0 eV), and MnO (3.10-3.90 eV). This reduction in band gap suggests a synergistic electronic interaction between the composite's constituents, which facilitates band-edge modification and promotes enhanced absorption of visible light. The narrower band gap of the prepared nanocomposite allows for higher absorption of visible light, which is crucial for practical photocatalytic applications that rely on solar energy. This bandgap enables our nanocomposite to effectively utilise the higher energy portion of the visible spectrum, directly impacting the generation of electron-hole pairs necessary for photocatalytic reactions.

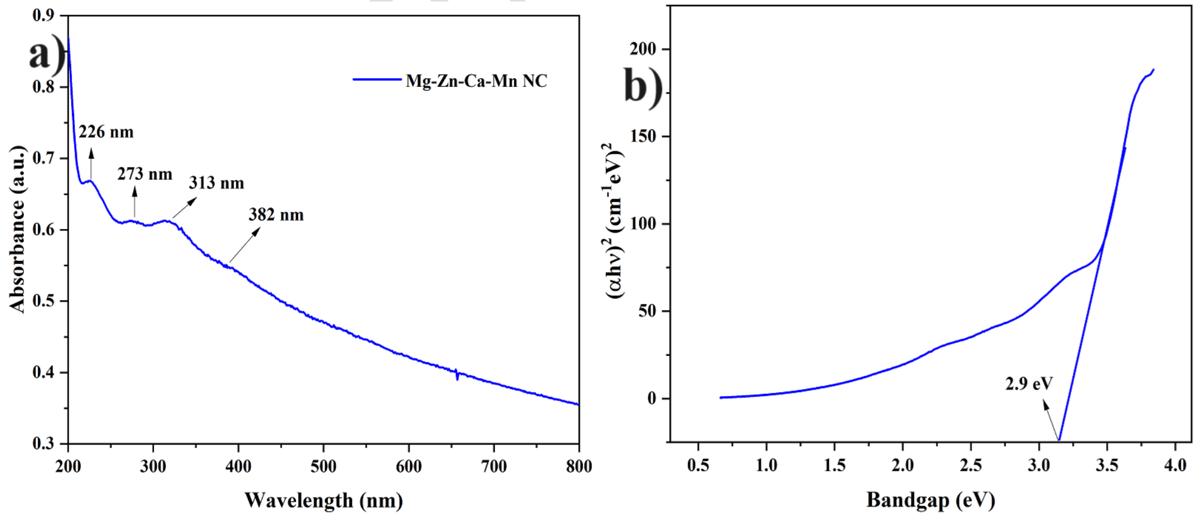

Figure 8. UV – vis spectrum and its bandgap for Mg-Zn-Ca-Mn nanocomposite

3.6. Luminescent property

The luminescence property of the nanocomposite was investigated through photoluminescence spectroscopy, with measurements taken at an excitation wavelength of 226 nm. The corresponding results are presented in Figure 9. Photoluminescence (PL) is widely recognised as a crucial area of investigation that offers valuable insights into crystal defects, surface effects, and material purity. The observed spectra display five distinct peaks at approximately 311, 370, 447, 562, and 622 nm. Based on the analysis of the PL data, it is evident that the prepared nanocomposite exhibits a polycrystalline nature. The UV emission peaks, observed at wavelengths of 311 and 370 nm, are attributed to the near-band-edge (NBE) emission of a metal oxide (Chin *et al.,* 2022).

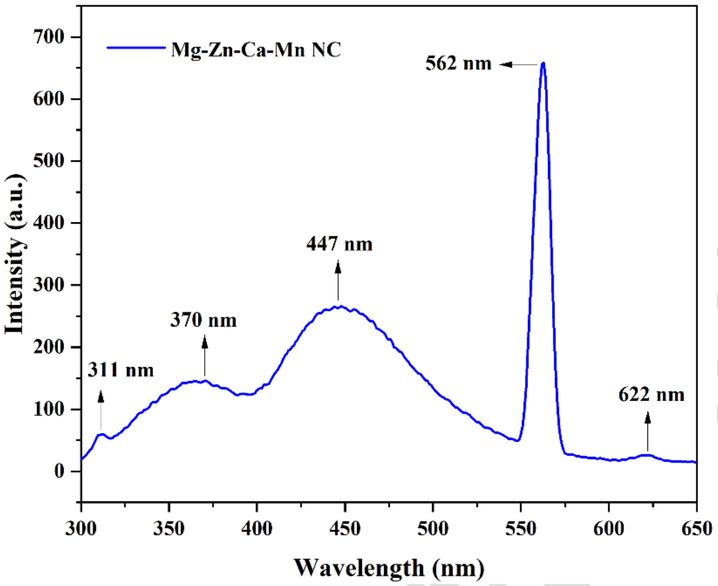

Figure 9. PL spectra of Mg-Zn-Ca-Mn nanocomposite

The NBE emissions observed in materials such as MgO, ZnO, and CaO are characteristic peaks. These peaks are attributed to radiative recombination, which occurs through a collision mechanism between an exciton. A weak intensity peak in the 360-370 nm range suggests a potential correlation with hydrogen impurities. The nanocomposite exhibits diverse emission peaks, predominantly located within the UV and visible regions, as indicated by the data. The presence of impurities or defects within the nanocomposite is responsible for the emission peaks observed in the visible region. The blue emission peak at 447 nm is believed to be caused by deep-level point defects, such as oxygen interstitials or vacancies (Vázquez-López *et al.,* 2022). The green emission observed at approximately 562 nm is attributed to oxygen's singly ionised charge state. The red emission peak observed at 622 nm is commonly associated with the transition caused by the presence of zinc interstitial (Zn_i) or oxygen interstitial (O_i) defect levels. Oxygen vacancies can act as shallow electron traps, delaying recombination of photoexcited electron–hole pairs and thereby extending the lifetime of charge carriers available for redox reactions. Defect states introduce intermediate energy levels within the band gap, enabling sub-band-gap photon absorption and extending the photocatalyst's spectral response into the visible range. Oxygen vacancies can serve as adsorption and activation sites for oxygen or pollutant molecules, thereby facilitating the generation of reactive oxygen species (ROS). Considering the discussion above, it can be inferred that Mg-Zn-Ca-Mn nanocomposites exhibit remarkable photocatalytic activity compared to other heterostructure photocatalyst systems.

3.7. Antioxidant activity

The DPPH free radical scavenging activity of the synthesised Mg-Zn-Ca-Mn nanocomposite (NC) was evaluated in comparison with ascorbic acid (Vitamin C), serving as the standard antioxidant, across concentrations ranging from 100 to 1000 µg/mL. The obtained results (Figure 10) reveal a clear concentration-dependent increase in scavenging efficiency for both the nanocomposite and the standard. At the lowest tested concentration (100 µg/mL), the nanocomposite exhibited 10.17% scavenging activity, which is markedly lower than that of Vitamin C (60.15%). This difference persisted at lower and intermediate concentrations, where Vitamin C consistently showed over 70% scavenging from 200 µg/mL onward, while the nanocomposite required a concentration above 600 µg/mL to exceed 50% activity.

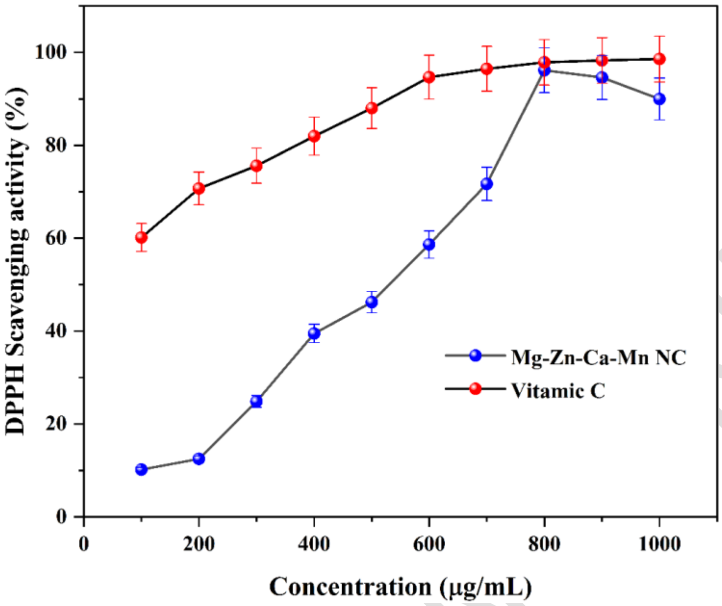

Figure 10. Antioxidant activity of Mg-Zn-Ca-Mn nanocomposite compared with vitamin C

A pronounced enhancement in the antioxidant performance of the nanocomposite was observed between 300 and 800 µg/mL, with scavenging activity increasing from 24.83% to 96.14%. Interestingly, the maximum activity for the nanocomposite (96.14%) was recorded at 800 µg/mL, after which a slight decline to 89.97% was observed at 1000 µg/mL. In contrast, Vitamin C demonstrated a steady increase in scavenging, reaching ~98% at 900 µg/mL, with negligible variation thereafter, indicating near-complete radical quenching at higher concentrations. The sharper slope in the nanocomposite's curve between 500 and 800 µg/mL suggests a threshold concentration where the active sites become sufficiently available for effective radical neutralisation.

The observed difference in scavenging efficiency at lower concentrations may be attributed to the intrinsic electron-donating ability and molecular mobility of Vitamin C, which allows rapid interaction with DPPH radicals. For the nanocomposite, the delayed onset of high activity could be related to factors such as the surface accessibility of active metal oxide sites, particle dispersion, and potential aggregation at lower concentrations, which can limit radical contact. However, at higher concentrations, the synergistic redox behaviour of Mg, Zn, Ca, and Mn oxides likely enhances electron transfer processes, resulting in scavenging efficiencies approaching that of Vitamin C. Additionally, the nanocomposite's surface area and particle size critically affect its antioxidant activity. Smaller particles with a larger surface area relative to their volume provide more reactive sites for capturing free radicals. Furthermore, the observed phenomenon can be attributed to the sharing of electron density between the oxygen atom of the prepared nanocomposite and the nitrogen atom in DPPH, specifically to the odd electron present at the nitrogen atom (Subramani, Ganeshan, et al., 2025). This transfer of electron density leads to an increase in the intensity of the n → π* transition at 517 nm wavelength. The antioxidant activity of the prepared nanocomposite was comparatively analysed with previously reported nanocomposites such as Fe2O3/C (83 %, 10 mg/mL), Cu-Zn-Mn (84.36 %, 500 µg/mL), and chitosan-encapsulated ZnFe2O4 (95.8 %, 1000 µg/mL), suggesting that with lower concentration, the maximum scavenging of DPPH was achieved with the nanocomposite prepared in this study. (Alam et al., 2022; Al-Rajhi et al., 2024; Bhattacharya et al., 2014)

3.8. Antibacterial activity

The antibacterial performance of the prepared nanocomposite towards Gram-negative (E. coli) and Gram-positive (S. aureus) bacteria using the Muller-Hinton agar method is depicted in Figure 11. The efficiency of the nanocomposite is compared with the standard antibacterial agent (Chlortetracycline (CT 30)) by varying the concentrations from 25 mg/mL to 100mg/mL. The antibacterial activity increases with the concentration of the nanocomposite, indicating a direct proportionality between concentration and antibacterial activity. The inhibition zones differ for both bacteria, as indicated by the standard, which shows 9 and 7 mm for *S. aureus* and *E. coli*, respectively. Similarly, the highest concentration of nanocomposite exhibits 15 and 13 nm for *S. aureus* and *E. coli*, respectively. This may be because the cell wall composition of Gram-negative bacteria is more compact compared to that of Gram-positive bacteria, which exhibit better resistance to antibacterial agents than Gram-negative bacteria. The higher antibacterial activity observed against Staphylococcus aureus compared to Escherichia coli can be attributed to fundamental differences in their cell wall architecture. S. aureus possesses a thick peptidoglycan layer (~20–80 nm) that is highly porous and lacks an outer membrane. This structure facilitates the easier penetration of reactive oxygen species (ROS), metal ions, or nanoparticle fragments generated by the nanocomposite, resulting in more efficient disruption of cellular integrity. Whereas E. coli has a thinner peptidoglycan layer (~7–8 nm) but is surrounded by an additional outer membrane composed of lipopolysaccharides (LPS). This outer membrane acts as a selective permeability barrier, hindering the diffusion of ROS, metal ions, and larger nanocomposite particles into the cell. Moreover, Gram-negative bacteria often possess more active efflux pumps that can expel toxic species before they reach lethal concentrations. The absence of an outer membrane in *S. aureus* enables direct and sustained interaction of the nanocomposite with the peptidoglycan and cytoplasmic membrane, whereas the protective LPS barrier in *E. coli* reduces the effective dose reaching critical cellular targets. The presence of multiple metal oxides impacts the enhanced antibacterial activity compared to standard agents. Multiple logical mechanisms exist for the inhibition of bacterial growth through the utilisation of nanoparticles. It has been postulated that nanocomposites exhibit an optimum interaction with bacterial cells, leading to the evolution of ROS. This, in turn, induces protein oxidation, lipid peroxidation, and DNA damage, ultimately culminating in bacterial cell death. Furthermore, it is worth noting that the nanocomposites produce metal ions such as (Ca^{2+}, Mg^{+}, Mn^{2+}, and Zn^{+}) that carry a positive charge. On the other hand, the bacterial cell membrane is negatively charged, leading to a direct interaction between the metallic ions and the membrane. This interaction has been observed to cause DNA damage. ROS generation contributes to oxidative stress within microbial cells, damaging multiple cellular components, including lipids, proteins, and DNA. On the other hand, the release of metal ions has been shown to disrupt microbial cell membranes and interfere with essential cellular processes by binding to proteins and enzymes, thereby inhibiting their function. Another potential factor to consider is the size, larger surface-to-volume ratio, and shape of nanocomposites. The size of the nanocomposite particles plays a critical role in determining their interaction with microbial cells and free radicals. Smaller particles have a higher surface area-to-volume ratio, providing more active interaction sites. This increased surface area enhances the nanocomposite's ability to interact with and penetrate microbial cell walls or to capture and neutralise free radicals more effectively. These characteristics may enhance the interaction between the nanocomposites and the bacterial cell membrane (Pachaiappan *et al.,* 2021).

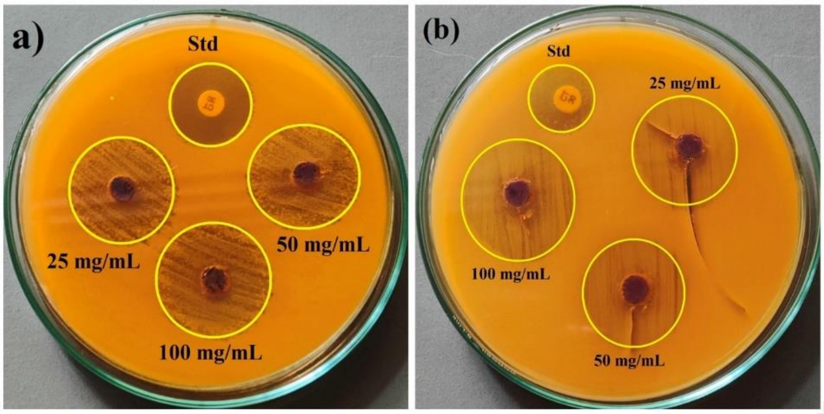

Figure 11. Antibacterial activity of Mg-Zn-Ca-Mn nanocomposite. a) S.*aureus* & b) *E.Coli*

Table 1. Antibacterial zone formation of nanocomposite against provided strains

Sample	**Inhibition zone (mm)**							
	S. aureus				***E. coli***			
	Concentration (mg/mL)							
	25	**50**	**100**	**std**	**25**	**50**	**100**	**std**
Mg-Zn-Ca-Mn NC	10	12	15	9	9	11	13	7

3.9. Photocatalytic performance

The photocatalytic characteristics of textile (Rhodamine B) and pharmaceutical pollutants (Amlodipine) in the availability of NC under sunlight irradiation are depicted in Figures 12 (a) and 14 (a). This graph displays the absorbance spectra of pollutants over time (0-90 minutes for Amlodipine and 0-60 minutes for Rhodamine B). The gradual decrease in absorbance intensity indicates that the nanocomposite actively degrades the pollutant, reducing its concentration in solution. The optical absorption has been analysed under various conditions, such as in the absence of light or a catalyst. The degradation of pollutants was revealed by the intensity of the decay of the characteristic peaks around 368 (Amlodipine) and 555 nm (Rhodamine B) as a function of irradiation time (t). The pollutants' absorption decreases gradually, indicating that the nanocatalyst effectively breaks down their molecules through a catalytic reaction. C/C_0 plot (Figure 12(b) and 14(b) shows the relative concentration of pollutants (C) compared to its initial concentration (C_0) over time for three cases: (i) Mg-Zn-Ca-Mn nanocomposite, (ii) without light and (iii) without catalyst. The Mg-Zn-Ca-Mn nanocomposite significantly lowers the C/C_0 ratio over time, demonstrating superior degradation efficiency compared to the control conditions. Figures 12(c) and 14(c) present the degradation percentage of pollutants degraded over time. The calculated degradation efficiency of the nanocomposite against Rhodamine B is 99.68 % within 60 mins, and Amlodipine is 98.55 % within 90 mins. The photocatalytic efficiency of various metal oxide composites against different pollutants is presented in Table 2.

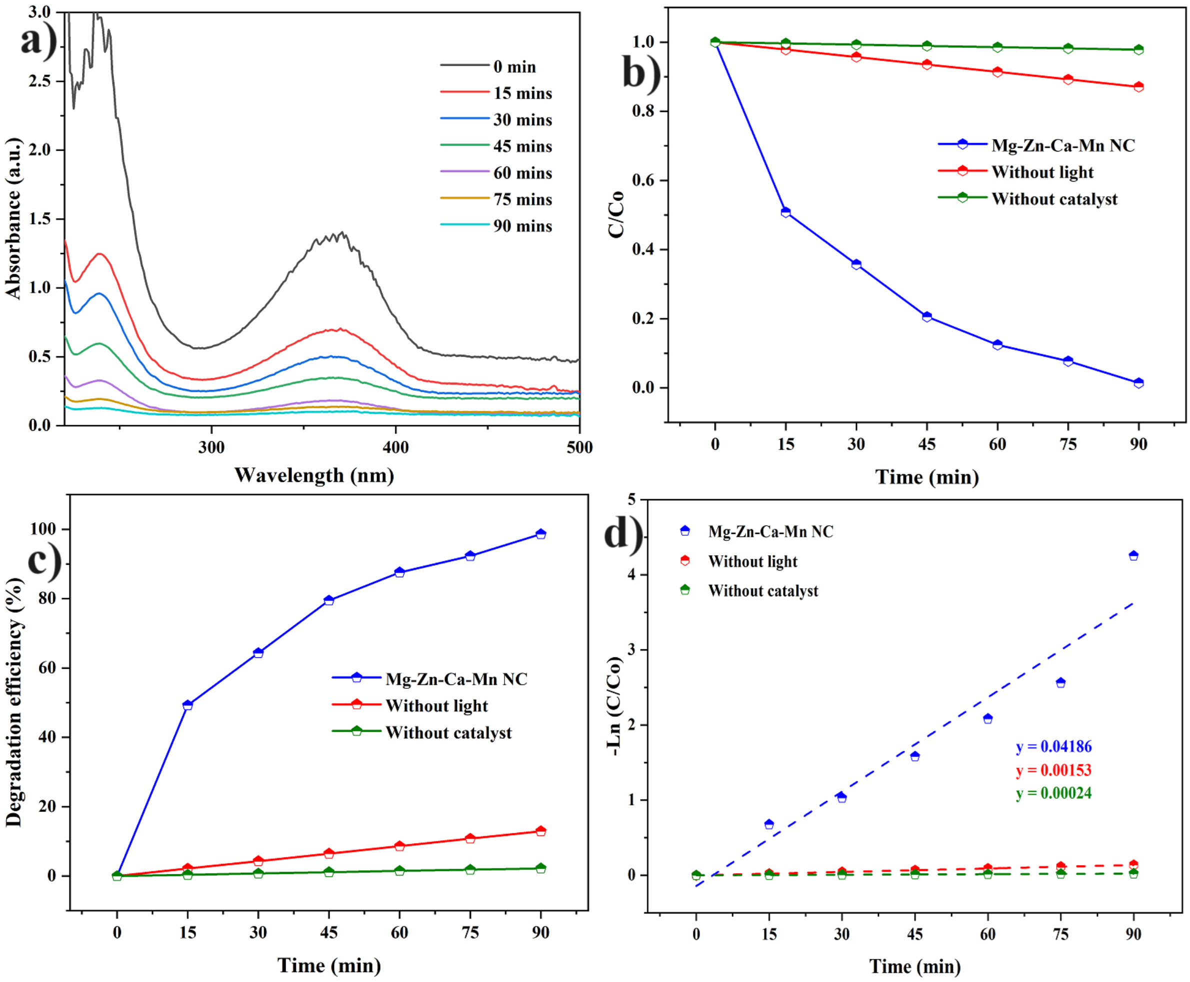

Figure 12. Photocatalytic performance on Amlodipine a) Time-dependent degradation, b) C/Co, c) degradation efficiency, and d) Pseudo first-order kinetics

Table 2. Photocatalytic activity of various metal composites towards various pollutants

Composite	Pollutant	Time (min)	Efficiency (%)	Ref
Zn-Mn-Mg	Methylene blue	75	89.1	(Subbiah *et al.*, 2021)
NiO-Fe_2O_3-CdO	Methyl orange	60	84.25	(Mukhtar *et al.*, 2020)
NiO-CdO-ZnO	Rhodamine B	99	60	(Wehbi *et al.*, 2023)
Mg-SiO_2-Zn	Chromium	120	72.75	(Galaburda *et al.*, 2024)
Mg-Cu0-WO_4/Bi_2WO_6	Rhodamine B	240	97.2	(Munawar *et al.*, 2021)
MgO–SnO_2	Sunset Yellow	60	99	(Shoran *et al.*, 2023)
Mn-Zn0-Mg-Fe_2O_4	Chloramine T	90	91	(Maksoud *et al.*, 2020)
TiO_2-Ag-ZnO	Methylene blue	60	25	(Tjardts *et al.*, 2023)
Fe_2O_3-Ag	Reactive red	120	99	(Huang-Mu *et al.*, 2023)
Mg-Zn-Ca-Mn NC	Rhodamine B	60	99	Present work
	Amlodipine	90	98	

The chemical structure of pharmaceutical pollutants is highly compatible with textile pollutants, which enables the nanocomposite to degrade Rhodamine B more quickly than Amlodipine. Rhodamine B and Amlodipine degradation without a catalyst is 2.1 and 1.8%, respectively, under sunlight. Similarly, the degradation efficiency with a photocatalyst under dark is 8.2 and 6.8 % for Rhodamine B and Amlodipine, indicating the pollutants' adsorption at the catalyst's surface. This adsorption phenomenon increases the degradation rate by enabling the adsorption and degradation simultaneously with sunlight stimulation. The analysis of pollutants without light and catalysts highlights the significance of both catalysts and sunlight for photocatalytic degradation.

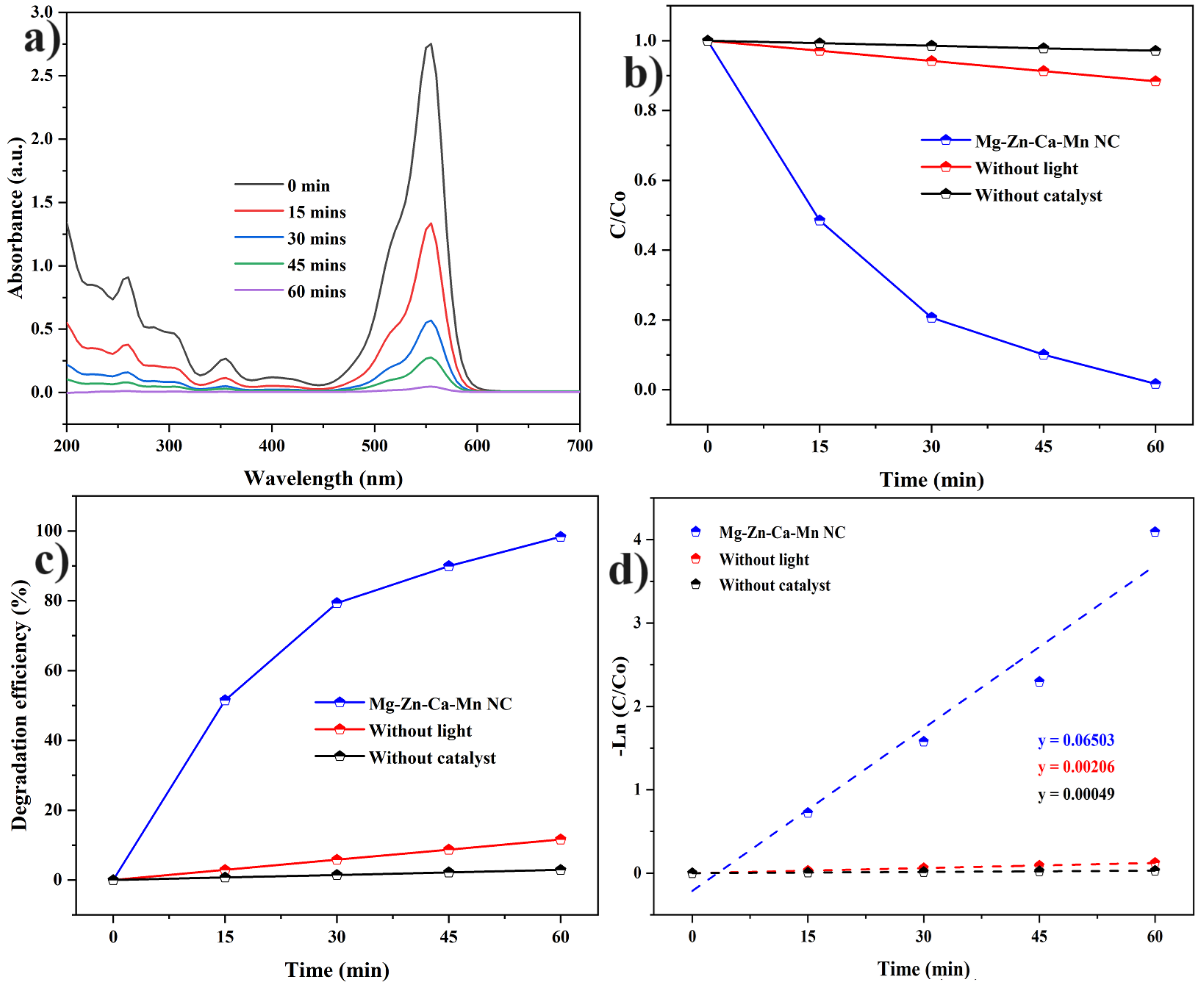

Figure 13. Photocatalytic performance on Rhodamine B: a) Time-dependent degradation, b) C/Co, c) degradation efficiency, and d) Pseudo first-order kinetics

Figures 12 and 13(d) show that photocatalytic degradation of produced nano catalysts against Rhodamine B and Amlodipine follows pseudo-first-order kinetic processes. Equation (5) examines the pseudo-first-order kinetics employing the Langmuir-Hinshelwood model. (Karthikeyan *et al.,* 2023).

$$Ln\frac{C}{Co} = kt \tag{5}$$

From the equation, the calculated degradation rate of Rhodamine B is 0.065, 0.002, and 0.0004 min^{-1} for nanocomposite, without light and catalyst, respectively. Similarly, the rates of amlodipine release are 0.041, 0.0015, and 0.0002 min-1 for the nanocomposite, without light, and with catalyst, respectively. The enhanced degradation rate is attributed to the presence of multiple nanoparticles in the composites, which adsorb pollutants and exhibit a high recombination rate.

4. Scavenging activity

Figure 14 shows the degradation efficiency response of each respective scavenger employed at a concentration of 5 mM. Notably, IPA and pBQ have drastically reduced the degradation efficiency of Rhodamine B and Amlodipine. This can be ascribed to the effective role of ROS species. OH and O_2^{*-} play a crucial role in the degradation of both pollutants, and their scavenging through IPA and pBQ leads to reduced degradation efficiency. Furthermore, the produced ROS species generally attack the chromophoric structure of pollutants, which significantly converts them into intermediate compounds, and further interaction leads to the mineralisation of pollutants. Thus, scavenging these species in the reaction system reduces the degradation efficiency of the pollutants. Photogenerated electrons and holes generally generate these scavenging species. Free h^+ and e^- have very short lifetimes in aqueous systems due to rapid trapping or recombination. Their indirect role via ROS provides a longer-lived oxidative/reductive pathway, thereby enhancing the reaction probability. However, the direct interaction between e^- and h^+ with pollutants is not observed as the degradation efficiency is minimally reduced with the scavenging of e^- and h^+ with $AgNO_3$ and AA.

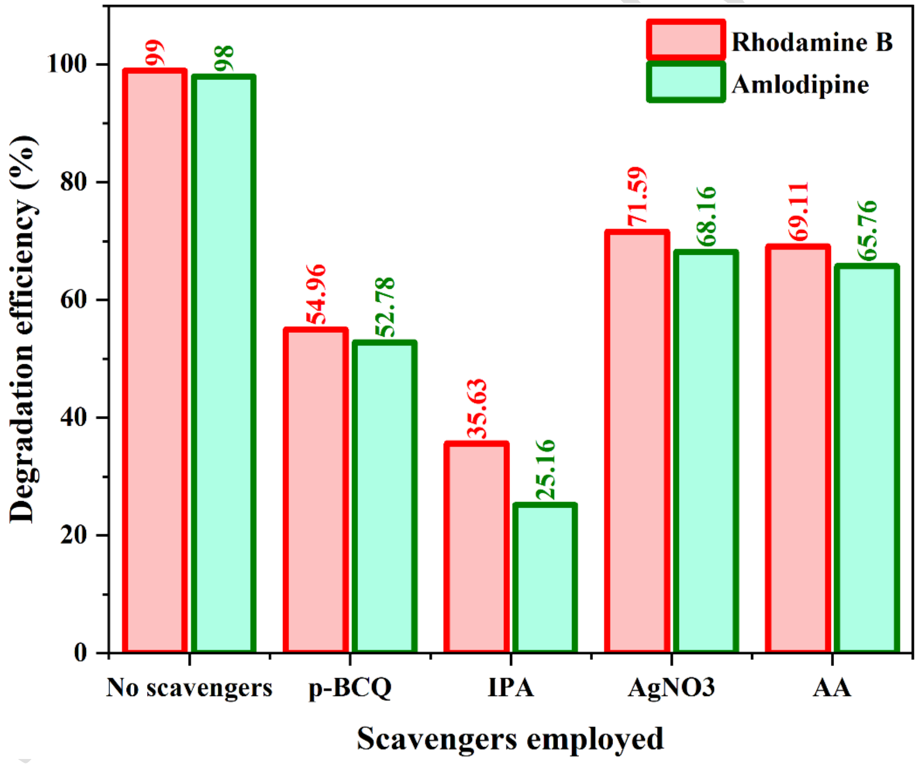

Figure 14. Evaluation of ROS responsible for the degradation of pollutants

4.1. Mechanism of degradation

The photocatalytic reaction primarily consists of four distinct steps (as seen in Figure 15): photoexcitation, ionisation of water, absorption of oxygen ions, and superoxide protonation. Upon light irradiation onto a semiconductor photocatalyst, the phenomenon of electron-hole pair generation ($e^{-}CB^{+}$ h^{+} VB) occurs (Subramani, Tamilselvi Mohanasundaram, et al., 2025). Beyond photoexcitation, the surface of the photocatalyst undergoes simultaneous oxidation and reduction reactions. The anticipated photodegradation mechanism of the Mg-Zn-Ca-Mn nanocomposite is as follows:

$$\text{Mg-Zn-Ca-Mn} + h\upsilon \longrightarrow \text{Mg-Zn-Ca-Mn}\ (e^-_{CB} + h^+_{VB}) \qquad (6)$$

Oxygen ion absorption:

$$\text{Mg-Zn-Ca-Mn}\ (e^-_{CB}) + O2 \longrightarrow \text{Mg-Zn-Ca-Mn} + {}^*O_2^- \qquad (7)$$

Ionisation of water:

$$H_2O \longrightarrow H^+ + {}^*OH \qquad (8)$$

$$^*O_2 + H^- \longrightarrow {}^*HO_2 \qquad (9)$$

Protonation of superoxide:

$$\text{Mg-Zn-Ca-Mn}\ (h^+_{VB}) + \text{pollutants} \longrightarrow \text{Degradation products} \qquad (10)$$

Oxidation:

$$HO^-_2 + H^+ \longrightarrow H_2O_2 \qquad (11)$$

Reduction:

$$HO_2^* + e^- \longrightarrow {}^*HO_2- \qquad (12)$$

It has been observed that when photogenerated electrons are present, they can undergo a reductive process in which they react with molecular oxygen. This reaction tends to create superoxide anion radicals, denoted as $^*O_2^-$. These radicals are considered to be less toxic compared to other reactive species.(Amor et al., 2024; Balamurugan et al., 2025; Serouti et al., 2024; Zohra et al., 2023).

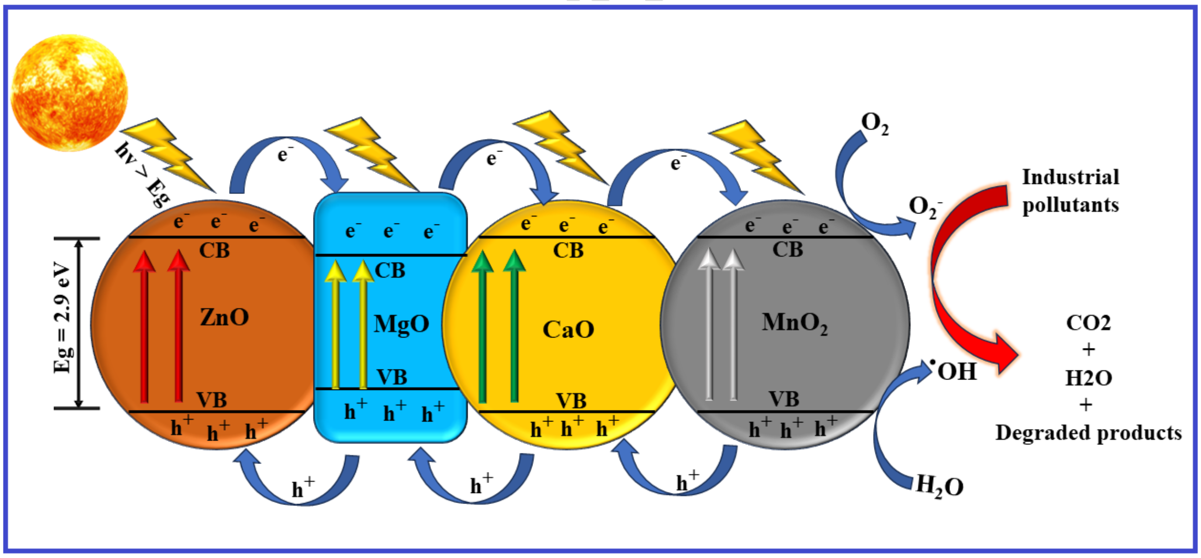

Figure 15. Photocatalytic degradation mechanism of Mg-Zn-Ca-Mn nanocomposite

The holes that are generated during the same process have been found to undergo an oxidative process. Specifically, they can interact with water molecules or hydroxyl ions. This reaction results in the evolution of highly reactive hydroxyl radicals, denoted as *OH. Overall, the photogenerated electrons and holes exhibit different reactivity patterns, with the electrons leading to the formation of less toxic superoxyanion radicals. In contrast, the holes generate highly reactive hydroxyl radicals. Upon interaction with superoxide anions, the electron-hole pairs undergo a reaction that leads to the formation of H_2O_2 (Kandasamy et al., 2023; Meneceur, Bouafia, Laouini, Mohammed, Daoudi, Hasan, et al., 2023; Salmi, Souhaila, et al., 2024; Wang et al., 2022). The utilisation of metal oxide combinations has resulted in the generation of highly active catalytic centres that significantly enhance the performance of photodegradation processes. A model proposed by A. Hezametal and Lei *et al.* (Hezam *et al.,* 2018) was utilised to gain insights into the process of electron-hole separation and its impact on boosted photocatalytic activity. According to the proposed mechanism, it is postulated that MgO is located between ZnO and CaO, with CaO positioned between ZnO and MnO_2. As a result, a repeating pattern of MgO and ZnO is formed, with all four oxides being close to each other within the nanocomposite. This arrangement gives rise to a heterostructure. Due to exposure to sunlight, the photoinduced electrons (e^-) originating from the conduction band (CB) of ZnO were observed to migrate to the CB of MnO_2, facilitated by the presence of MgO and CaO, which possess a positive CB.

Concurrently, the photogenerated holes (h^+) undergo transfer from the valence band (VB) of MnO_2 to the VB of ZnO through the intermediation of CaO and MgO, facilitated by the negative VB (Devabharathi *et al.,* 2024; Gharbi *et al.,* 2023; Hasan, *et al.,* 2024; Hasan, *et al.,* 2024; Meneceur, *et al.,* 2023). The presence of these properties has hindered the recombination process of electron-hole pairs by prolonging the lifespan of the charge carriers *(Mohammed et al.,* 2024; Son *et al.,* 2021). The degradation of Amlodipine in a photocatalytic process primarily involves the cleavage of its dihydropyridine ring, leading to the formation of various intermediate products, including but not limited to pyridine and simpler organic compounds. These transformations typically occur through reactions initiated by hydroxyl radicals and other ROS, which abstract electrons from or add to the organic molecules, destabilising bonds and leading to fragmentation. For Rhodamine B, degradation usually starts with the cleavage of the ethylamine side chains, followed by the opening of the xanthene ring structure. The process generates several aromatic intermediates, which further degrade into smaller carboxylic acids and eventually into carbon dioxide and water under optimal conditions. This pathway is facilitated by the formation of hydroxyl and superoxide radicals on the photocatalyst's surface. The improved photocatalytic activity of the Mg-Zn-Ca-MnO_2 nanocomposite revealed that its effectiveness can be attributed to the efficient separation of photoinduced holes and electrons. This separation is achieved by transmitting holes and electrons across the contact boundary among MgO, ZnO, CaO, and MnO_2. Moreover, a double heterojunction within the synthesised nanocomposite presents a promising option for enhancing the photocatalytic activity (Goktas & Goktas, 2021).

5. Stability and reusability

A series of reusability experiments were conducted to investigate the cycling durability of the composite photocatalyst. The investigation into the stability of the nanocomposite was conducted following five consecutive runs of photocatalytic experiments, using identical experimental conditions as those employed for the recycled nanocomposite. Following each run, the photocatalyst was isolated from the solution through centrifugation. Subsequently, it underwent two rounds of washing with deionised water and ethanol, followed by drying to prepare it for subsequent utilisation.

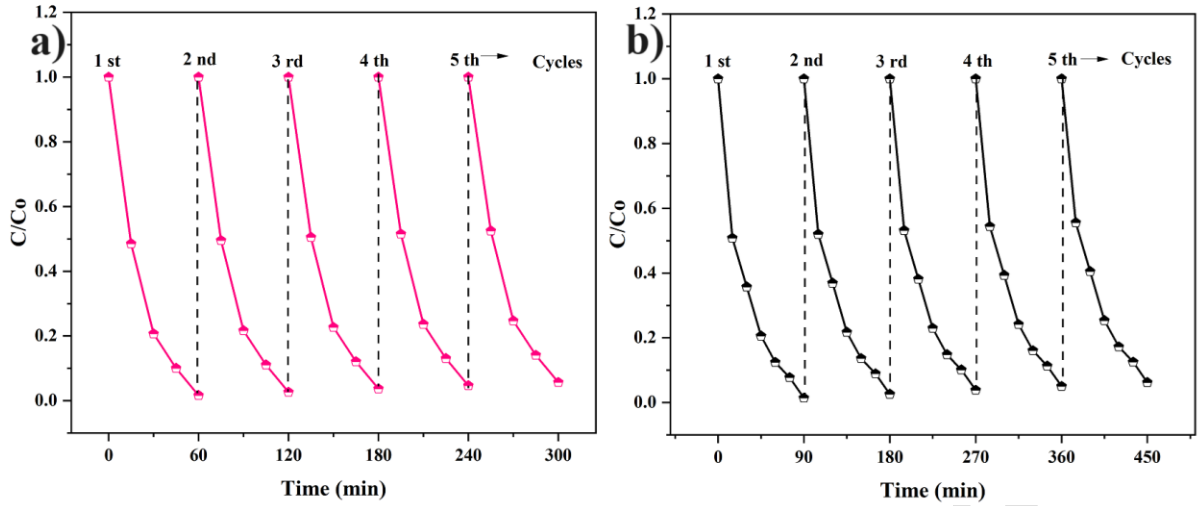

Figure 16. Stability of Mg-Zn-Ca-Mn nanocomposite against Rhodamine B (a) and Amlodipine (b)

The sustained photocatalytic activity of the nanocomposite was observed even after undergoing five consecutive runs, and it is only reduced by 4.1% for Rhodamine B and 5.3% for Amlodipine, indicating the excellent stability of the nanocomposite towards industrial pollutants (Figure 16). The high stability of a nanocomposite after photocatalytic activity is due to its strong structural integrity, which resists degradation during cycles, and the robust interaction between its components, preventing phase separation or leaching (Rani *et al.,* 2023). Additionally, resistance to photo corrosion, surface passivation to minimise defects, and high oxidation resistance contribute to its durability. The rod morphology of the MgO in the composite, which enables it to withstand harsh environmental conditions, also plays a critical role in maintaining stability over extended use. The stability also reveals that the nanocomposite's crystalline, functional, and morphological properties remain unchanged after five cycles. Preparation of Mg-Zn-Ca-Mn nanocomposite is an eco-friendly and straightforward method with excellent crystalline properties. A high-quality nanocomposite with enhanced physicochemical properties has been prepared in a very short period. The sol-gel process has been utilised, and the cost required for producing the nanocomposite is comparatively low. The prepared nanocomposite effectively eliminates industrial pollutants in a short period, meeting market demand. The combination of metals, particularly Zn and Mg, can impart antimicrobial properties, making the nanocomposite suitable for treating water contaminated with microorganisms. Using Ca and Mg in the composite generally enhances the biocompatibility, making it safer for environmental applications without introducing harmful by-products. These nanocomposites are known for their structural integrity and can withstand harsh environmental conditions. Adding Mn provides mechanical strength and stability, crucial for long-term ecological remediation. All nanomaterials are involved in photocatalytic activity, which enables the effective transfer of electrons and reduces the recombination rate, thereby boosting the degradation process. From the above discussions, it has been observed that the prepared Mg-Zn-Ca-Mn nanocomposite could be an environmentally friendly material for various applications.

6. Conclusion

The highly effective photocatalyst has been prepared through the sol-gel method by combining the precursors of Mg, Zn, Ca, and Mn and reduced by NaOH simultaneously. The XRD results indicate the nanocomposite's crystalline nature and excellent structural properties, with an average crystallite size of 19.74 nm. The various functional groups and metal presence have been confirmed using FTIR. The FESEM reveals the formation of rod morphology of MgO and spherical morphology of ZnO, CaO, and MnO_2, which surrounds the rod. The EDAX and XRD represent the formation and high purity of Mg-Zn-Ca-Mn nanocomposite. The particle size of the nanocomposite is 36.64 nm, which also aligns with the crystalline size calculated from the XRD observations. Optical analysis revealed a favourable bandgap of 2.9 eV, enabling efficient photocatalytic degradation under sunlight. Precisely, 99.68% degradation of Rhodamine B was achieved in 60 minutes and 98.55% degradation of Amlodipine in 90 minutes, surpassing the existing reports. The nanocomposite exhibited potent antibacterial activity, significantly inhibiting the growth of both *S. aureus* (15 mm) and *E. coli* (13 mm). Moreover, its antioxidant performance stabilised DPPH radicals with a scavenging efficiency of 97.45%, demonstrating its capability in neutralising reactive oxygen species (ROS). Stability studies revealed minimal efficiency loss (4.1% for Rhodamine B, 5.3% for Amlodipine) after five cycles, demonstrating its durability for repeated use. The combination of ZnO, MgO, CaO, and MnO_2 facilitated enhanced pollutant degradation, antimicrobial efficacy, and antioxidant activity, offering a promising, eco-friendly nanomaterial for wastewater treatment. Despite its promising results, some limitations remain in this study. Our work focused on sunlight-assisted degradation, but further research is needed to evaluate its performance under different light sources, such as LED or UV irradiation. Although the nanocomposite retains efficiency after five cycles, extended durability studies beyond laboratory conditions are necessary to assess its real-world applicability. Moreover, incorporating tests against MDR bacterial strains in future studies would significantly strengthen the evaluation of the Mg-Zn-Ca-Mn nanocomposite's biocidal potential. Additionally, exploring its mechanism of bacterial inhibition in MDR strains, such as ROS generation, membrane disruption, and ion exchange, could help refine its composition for enhanced performance. Future studies could also compare its effectiveness with conventional disinfectants to highlight its advantages in environmental and biomedical applications.

References

Abdel Maksoud, M. I. A., El-Sayyad, G. S., El-Khawaga, A. M., Abd Elkodous, M., Abokhadra, A., Elsayed, M. A., Gobara, M., Soliman, L. I., El-Bahnasawy, H. H., & Ashour, A. H. (2020). Nanostructured Mg substituted Mn-Zn ferrites: A magnetic recyclable catalyst for outstanding photocatalytic and antimicrobial potentials. *Journal of Hazardous Materials*, *399*(123000), 123000. https://doi.org/10.1016/j.jhazmat.2020.123000

Abdipour, H., Asgari, G., Seid-Mohammadi, A., Rahmani, A., & Shokoohi, R. (2024). Investigating the efficiency of fixed bed column containing Fe3O4-ZIF8@eggshell membrane matrix in concurrent adsorption of arsenic and nitrate from water. *Ecotoxicology and Environmental Safety*, *288*(117359), 117359. https://doi.org/10.1016/j.ecoenv.2024.117359

Abdipour, H., & Hemati, H. (2024). Sonocatalytic process of penicillin removal using - Fe2O3 / effect of different parameters / degradation mechanism/ kinetic study/optimisation with response surface model. *International Journal of Environmental Analytical Chemistry*, *104*(20), 8617–8638. https://doi.org/10.1080/03067319.2023.2207465

Al Sdran, N., Chandekar, K. V., Shkir, M., & Ali, H. E. (2024). Tuning the structural, morphological, optical, dielectric, and magnetic properties of PVA via embedding with CoFe2O4:CuO nanoparticles. *Ceramics International*. https://doi.org/10.1016/j.ceramint.2024.11.035

Alam, M. W., Al Qahtani, H. S., Souayeh, B., Ahmed, W., Albalawi, H., Farhan, M., Abuzir, A., & Naeem, S. (2022). Novel copper-zinc-manganese ternary metal oxide nanocomposite as heterogeneous catalyst for glucose sensor and antibacterial activity. *Antioxidants (Basel, Switzerland)*, *11*(6), 1064. https://doi.org/10.3390/antiox11061064

Al-Rajhi, A. M. H., Abdelghany, T. M., Almuhayawi, M. S., Alruhaili, M. H., Al Jaouni, S. K., & Selim, S. (2024). The green approach of chitosan/Fe2O3/ZnO-nanocomposite synthesis with an evaluation of its biological activities. *Applied Biological Chemistry*, *67*(1). https://doi.org/10.1186/s13765-024-00926-2

Amor, I. B., Hemmami, H., Laouini, S. E., Ahmed, S., Mohammed, H. A., Abdullah, J. A. A., Azooz, E. A., Al-Mulla, E. A. J., & Alharthi, F. (2024). Enhancing oxidant and dye scavenging through MgO-based chitosan nanoparticles for potential antioxidant coatings and efficient photocatalysts. *Biomass Conversion and Biorefinery*, *14*(24), 32343–32357. https://doi.org/10.1007/s13399-023-04923-1

Asgari, G., Seid-Mohammadi, A., Rahmani, A., Shokoohi, R., & Abdipour, H. (2024). Concurrent elimination of arsenic and nitrate from aqueous environments through a novel nanocomposite: Fe3O4-ZIF8@eggshell membrane matrix. *Journal of Molecular Liquids*, *411*(125810), 125810. https://doi.org/10.1016/j.molliq.2024.125810

Balamurugan, A., Suresh, K. C., Jagan, K. S. G., Sivagurunathan, G. S., Marnadu, R., Naren Vidaarth, T. M., Surendhiran, S., & Khadar, Y. A. S. (2025). Detoxification of textile industry effluents using SnO2/carbon dots nanocomposites synthesised by green fabrication using Moringa leaves extract. *Journal of Materials Science: Materials in Electronics*, *36*(18). https://doi.org/10.1007/s10854-025-15171-6

Barani, D., Bouafia, A., Laouini, S. E., Tedjani, M. L., Alharthi, F., Sonia, M.-T., & Trzepieciński, T. (2025). Enhanced antioxidant, anti-inflammatory, and photocatalytic properties of α-tocopherol-coated copper oxide nanoparticles: synthesis, characterisation, and multifunctional applications. *International Journal of Food Science & Technology*, *60*(1). https://doi.org/10.1093/ijfood/vvaf051

Bhattacharya, K., Gogoi, B., Buragohain, A. K., & Deb, P. (2014). Fe_2O_3/C nanocomposites having distinctive antioxidant activity and hemolysis prevention efficiency. *Materials Science & Engineering. C, Materials for Biological Applications*, *42*, 595–600. https://doi.org/10.1016/j.msec.2014.05.062

Bokuniaeva, A. O., & Vorokh, A. S. (2019). Estimation of particle size using the Debye equation and the Scherrer formula for polyphasic TiO2 powder. *Journal of Physics. Conference Series*, *1410*(1), 012057. https://doi.org/10.1088/1742-6596/1410/1/012057

Chen, G., Roy, I., Yang, C., & Prasad, P. N. (2016). Nanochemistry and nanomedicine for nanoparticle-based diagnostics and therapy. *Chemical Reviews*, *116*(5), 2826–2885. https://doi.org/10.1021/acs.chemrev.5b00148

Chin, Y.-H., Sin, J.-C., Lam, S.-M., Zeng, H., Lin, H., Li, H., & Mohamed, A. R. (2022). 0-D/3-D heterojunction composite constructed by decorating transition metal oxide nanoparticle on peony-like ZnO hierarchical microstructure for improved photodegradation of palm oil mill effluent. *Optik*, *260*(169098), 169098. https://doi.org/10.1016/j.ijleo.2022.169098

Dave, S., Das, J., Varshney, B., & Sharma, V. P. (2022). Dyes and pigments: Interventions and how safe and sustainable are colors of life!!! In *Environmental Science and Engineering* (pp. 1–20). Springer International Publishing. https://doi.org/10.1007/978-3-031-08991-6_1

Delavari, M., Beyranvand, F., Jahangiri, M., & Abdipour, H. (2024). Increasing the permeability of carbon dioxide and nitrogen gases through a polymer membrane consisting of a modified polyether block amide and experimental design. *Journal of Polymers and the Environment*, *32*(10), 4822–4841. https://doi.org/10.1007/s10924-024-03247-z

Devabharathi, V., Jagan, K. S. G., Priyan, S. R., Vidaarth, T. M. N., Surendhiran, S., Khadar, Y. A. S., & Kandasamy, K. (2024). Rational design of NiO nanoflakes and porous GCN nanocomposite for synergic effectiveness on photocatalytic degradation of industry effluents and biological activity. *Chemical Physics Impact*, *8*(100637), 100637. https://doi.org/10.1016/j.chphi.2024.100637

Dontsova, T. A., Nahirniak, S. V., & Astrelin, I. M. (2019). Metaloxide nanomaterials and nanocomposites of ecological purpose. *Journal of Nanomaterials*, *2019*, 1–31. https://doi.org/10.1155/2019/5942194

Elimination of nickel and chromium(VI) ions from industerial wastewater by electrodialysis/characteristics/impact of parameters. (2024). *Global NEST Journal*, 1–11. https://doi.org/10.30955/gnj.005098

Fang, L., Zhang, B., Li, W., Li, X., Xin, T., & Zhang, Q. (2014). Controllable synthesis of ZnO hierarchical architectures and their photocatalytic property. *Superlattices and Microstructures*, *75*, 324–333. https://doi.org/10.1016/j.spmi.2014.03.001

Feng, L., Yang, Y., Zhao, Y., Ma, K., & Cui, J. (2024). Corrosion behaviors and mechanism of AlxCrFeMnCu high-entropy alloys in a 3.5 wt% NaCl solution. *Corrosion Science*, *233*(112087), 112087. https://doi.org/10.1016/j.corsci.2024.112087

Galaburda, M., Sternik, D., Chrzanowska, A., Oranska, O., Kovalov, Y., & Derylo-Marczewska, A. (2024). Physicochemical and adsorption characterisation of char derived from resorcinol-formaldehyde resin modified with metal oxide/silica nanocomposites. *Materials*, *17*(9). https://doi.org/10.3390/ma17091981

Gautam, V., Srivastava, A., Singh, K. P., & Yadav, V. L. (2016). Vibrational and gravimetric analysis of polyaniline/polysaccharide composite materials. *Polymer Science Series A*, *58*(2), 206–219. https://doi.org/10.1134/s0965545x16020085

Gavrilescu, M. (2021). Water, soil, and plants interactions in a threatened environment. *Water*, *13*(19), 2746. https://doi.org/10.3390/w13192746

Gharbi, A. H., Hemmami, H., Laouini, S. E., Amor, I. B., Zeghoud, S., Amor, A. B., Alharthi, F., Barhoum, A., & Abdullah, J. A. A. (2023). Green synthesis of ZnO@SiO2 nanoparticles using Calligonum comosum L. extract: an efficient approach for organic pollutant degradation in wastewater. *Biomass Conversion and Biorefinery*. https://doi.org/10.1007/s13399-023-05063-2

Gharbi, A. H., Hemmami, H., Laouini, S. E., Bouafia, A., Ben Amor, I., Zeghoud, S., Gherbi, M. T., Ben Amor, A., Alharthi, F., & Abdullah, J. A. A. (2024). Novel CuO–SiO2 nanocomposites: synthesis, kinetics, recyclability, high stability and photocatalytic efficiency for Rose Bengal dye removal. *Transition Metal Chemistry*, *49*(3), 195–213. https://doi.org/10.1007/s11243-024-00574-x

Goktas, S., & Goktas, A. (2021). A comparative study on recent progress in efficient ZnO based nanocomposite and heterojunction photocatalysts: A review. *Journal of Alloys and Compounds*, *863*(158734), 158734. https://doi.org/10.1016/j.jallcom.2021.158734

Gong, C., Zheng, Z., Dong, F., & Wang, Z. (2023). Survey of microbial contamination levels of direct drinking water from terminal devices in Yantai City. *Pollution Study*, *4*(1). https://doi.org/10.54517/ps.v4i1.2071

Goodarzi, S., Torabideh, M., Parsaseresht, G., Abdipour, H., Kamani, H., & Zomorrodi Jangaee, T. (2024). Penicillin removal from the aqueous environment based on AOPs/challenges and outlook. A review. *Applied Water Science*, *14*(7). https://doi.org/10.1007/s13201-024-02223-1

Hasan, G. G., Laouini, S. E., Osman, A. I., Bouafia, A., Althamthami, M., Meneceur, S., Al-Hazeef, M. S. F., Al-Fatesh, A. S., & Rooney, D. W. (2024). Green synthesis of Mn3O4@CoO nanocomposites using Rosmarinus officinalis L. extract for enhanced photocatalytic hydrogen production and CO2 conversion. *Journal of Environmental Chemical Engineering*, *12*(5), 113911. https://doi.org/10.1016/j.jece.2024.113911

Hasan, G. G., Laouini, S. E., Osman, A. I., Bouafia, A., Althamthami, M., Meneceur, S., Kir, I., Mohammed, H., Lumbers, B., & Rooney, D. W. (2024). Nanostructured Mn@NiO composite for addressing multi-pollutant challenges in petroleum-contaminated water. *Environmental Science and Pollution Research International*, *31*(31), 44254–44271. https://doi.org/10.1007/s11356-024-34012-3

Hassan, S. E.-D., Fouda, A., Saied, E., Farag, M. M. S., Eid, A. M., Barghoth, M. G., Awad, M. A., Hamza, M. F., & Awad, M. F. (2021). Rhizopus oryzae-mediated green synthesis of magnesium oxide nanoparticles (MgO-NPs): A promising tool for antimicrobial, mosquitocidal action, and tanning effluent treatment. *Journal of Fungi (Basel, Switzerland)*, *7*(5), 372. https://doi.org/10.3390/jof7050372

Hezam, A., Namratha, K., Drmosh, Q. A., Ponnamma, D., Nagi Saeed, A. M., Ganesh, V., Neppolian, B., & Byrappa, K. (2018). Direct Z-scheme Cs_2O–Bi_2O_3–ZnO heterostructures for photocatalytic overall water splitting. *Journal of Materials Chemistry. A, Materials for Energy and Sustainability*, *6*(43), 21379–21388. https://doi.org/10.1039/c8ta08033j

Huang-Mu, L., Devanesan, S., Farhat, K., Kim, W., & Sivarasan, G. (2023). Improving the efficiency of metal ions doped Fe2O3 nanoparticles: Photocatalyst for removal of organic dye from aqueous media. *Chemosphere*, *337*, 139229. https://doi.org/10.1016/j.chemosphere.2023.139229

Jonidi Jafari, A., Jafari Mansoorian, H., Askarpour, H., Salari, M., Eslami, F., Faraji, M., Shomoossi, F., Abdipour, H., & Jaberi Ansari, F. (2024). Analysing and optimising the adsorption of metronidazole antibiotic on nano-scale pumice mine waste based RSM-CCD technique in water. *International Journal of Environmental Science and Technology: IJEST*. https://doi.org/10.1007/s13762-024-06102-9

Kamani, H., Hosseinzehi, M., Ghayebzadeh, M., Azari, A., Ashrafi, S. D., & Abdipour, H. (2024). Degradation of reactive red 198 dye from aqueous solutions by combined technology advanced sonofenton with zero valent iron: Characteristics/ effect of parameters/kinetic studies. *Heliyon*, *10*(1), e23667. https://doi.org/10.1016/j.heliyon.2023.e23667

Kandasamy, K., Surendhiran, S., Jagan, K. S. G., Kumar, G. S., Khadar, Y. A. S., & Rajasingh, P. (2023). Green synthesis of CdS Quantum dots for photocatalytic and anti-corrosive applications in aqueous media. *Applied Surface Science Advances*, *13*(100364), 100364. https://doi.org/10.1016/j.apsadv.2022.100364

Karthikeyan, S., Dhanakodi, K., Surendhiran, S., Jagan, K. S. G., Lenin, N., Dhatchinamurthy, L., & Rajamanickam, A. T. (2023). Sonochemical synthesis of Sn-doped La2O3 nanoparticles and its application for the photocatalytic degradation of hazardous pollutants. *Journal of Materials Science: Materials in Electronics*, *34*(14). https://doi.org/10.1007/s10854-023-10561-0

Karthikeyan, S., Dhanakodi, K., Surendhiran, S., Jagan, K. S. G., Thirunavukkarasu, P., & Arunraja, L. (2023). Effect of synthesis parameters on the structural, morphological characteristics, and photocatalytic activity of La2O3 nanoparticles. *Journal of the Indian Chemical Society*, *100*(1), 100860. https://doi.org/10.1016/j.jics.2022.100860

Khalooei, M., Torabideh, M., Rajabizadeh, A., Zeinali, S., Abdipour, H., Ahmad, A., & Parsaseresht, G. (2024). Evaluating the efficiency of zeolitic imidazolate framework-67(ZIF-67) in elimination of arsenate from aqueous media by response surface methodology. *Results in Chemistry*, *11*(101811), 101811. https://doi.org/10.1016/j.rechem.2024.101811

Khan, L., Ikram, M., Haider, A., Shahzadi, A., Ul-Hamid, A., Ullah, H., Khan, S., Algaradah, M. M., Abd-Rabboh, H. S. M., Nabgan, W., & Shahzadi, I. (2023). Carbon spheres/polyvinylpyrrolidone doped MnO2 nanorods served as dye degrader and antibacterial activity with evidential molecular docking. *Surfaces and Interfaces*, *42*(103372), 103372. https://doi.org/10.1016/j.surfin.2023.103372

Khan, N. A., Singh, S., López-Maldonado, E. A., Pavithra, Méndez-Herrera, P. F., López-López, J. R., Baig, U., Ramamurthy, P. C., Mubarak, N. M., Karri, R. R., & Aljundi, I. H. (2023). Emerging membrane technology and hybrid treatment systems for the removal of micropollutants from wastewater. *Desalination*, *565*(116873), 116873. https://doi.org/10.1016/j.desal.2023.116873

Kir, I., Mohammed, H. A., Laouini, S. E., Souhaila, M., Hasan, G. G., Abdullah, J. A. A., Mokni, S., Naseef, A., Alsalme, A., & Barhoum, A. (2024). Plant extract-mediated synthesis of CuO nanoparticles from lemon peel extract and their modification with polyethylene glycol for enhancing photocatalytic and antioxidant activities. *Journal of Polymers and the Environment*, *32*(2), 718–734. https://doi.org/10.1007/s10924-023-02976-x

Legmairi, S., Meneceur, S., Hasan, G. G., Eddine, L. S., Mohammed, H. A., Alharthi, F., & Abdullah, J. A. A. (2023). Enhanced photocatalytic activity and antiviral evaluation of CuO@Fe2O3NC for amoxicillin degradation and SARS-CoV-2 treatment. *Nanotechnology*, *34*(44). https://doi.org/10.1088/1361-6528/acebfa

Locatelli, M., Gindro, R., Travaglia, F., Coïsson, J.-D., Rinaldi, M., & Arlorio, M. (2009). Study of the DPPH-scavenging activity: Development of a free software for the correct interpretation of data. *Food Chemistry*, *114*(3), 889–897. https://doi.org/10.1016/j.foodchem.2008.10.035

Maravelaki-Kalaitzaki, P. (2005). Black crusts and patinas on Pentelic marble from the Parthenon and Erechtheum (Acropolis, Athens): characterisation and origin. *Analytica Chimica Acta*, *532*(2), 187–198. https://doi.org/10.1016/j.aca.2004.10.065

Meneceur, S., Bouafia, A., Laouini, S. E., Mohammed, H. A., Daoudi, H., Chami, S., Hasan, G. G., Abdullah, J. A. A., & Salmi, C. (2023). Removal efficiency of heavy metals, oily in water, total suspended solids, and chemical oxygen demand from industrial petroleum wastewater by modern green nanocomposite methods. *Journal of Environmental Chemical Engineering*, *11*(6), 111209. https://doi.org/10.1016/j.jece.2023.111209

Meneceur, S., Bouafia, A., Laouini, S. E., Mohammed, H. A., Daoudi, H., Hasan, G. G., & Salmi, C. (2023). High-efficiency photocatalytic degradation of antibiotics and molecular docking study to treat the omicron variant of COVID-19 infection using biosynthesised $ZnO@Fe_3O_4$ nanocomposites. *Physica Scripta*, *98*(11), 115926. https://doi.org/10.1088/1402-4896/acff2d

Meneceur, S., Laouini, S. E., Ali Mohammed, H., Bouafia, A., Salmi, C., Ahmed Abdullah, J. A., & Alharthi, F. (2025). Eco-Friendly ZnO/CuO/Ni Nanocomposites: Enhanced photocatalytic dye adsorption and hydrogen evolution for sustainable energy and water purification. *Journal of Crystal Growth*, *650*(127984), 127984. https://doi.org/10.1016/j.jcrysgro.2024.127984

Moein, H., Nakhaei, S., Norabadi, E., Kamani, H., & Abdipour, H. (2025). Investigating the photocatalytic removal of amoxicillin from aqueous solutions by $Fe\text{-}TiO_2@Fe_3O_4$ magnetic nanoparticles. Characteristics/effect of parameters/kinetic study. *Chemical Engineering Communications*, *212*(7), 1031–1047. https://doi.org/10.1080/00986445.2024.2445230

Mohammed, H. A., Laouini, S. E., Meneceur, S., Salmi, C., & Husein, M. M. (2024). MgO/Ni nanocomposite and its PVP-modified derivative for catalytic CO2 methanation and photocatalytic hydrogen production. *Surfaces and Interfaces*, *51*(104643), 104643. https://doi.org/10.1016/j.surfin.2024.104643

Mourdikoudis, S., Kostopoulou, A., & LaGrow, A. P. (2021). Magnetic nanoparticle composites: Synergistic effects and applications. *Advanced Science (Weinheim, Baden-Wurttemberg, Germany)*, *8*(12), 2004951. https://doi.org/10.1002/advs.202004951

Mu, Y., Liu, L., Shi, J., Sun, T., Hu, K., Jia, Y., Song, K., Jia, Y., Wang, Q., & Wang, G. (2022). Multi-type dislocation substructure evolution in a high-strength and ductile duplex high-entropy nanocomposites. *Composites. Part B, Engineering*, *247*(110322), 110322. https://doi.org/10.1016/j.compositesb.2022.110322

Mukhtar, F., Munawar, T., Nadeem, M. S., Hasan, M., Hussain, F., Nawaz, M. A., & Iqbal, F. (2020). Multi metal oxide NiO-Fe2O3-CdO nanocomposite-synthesis, photocatalytic and antibacterial properties. *Applied Physics. A, Materials Science & Processing*, *126*(8). https://doi.org/10.1007/s00339-020-03776-z

Munawar, T., Iqbal, F., Yasmeen, S., Mahmood, K., & Hussain, A. (2020). Multi metal oxide NiO-CdO-ZnO nanocomposite–synthesis, structural, optical, electrical properties and enhanced sunlight driven photocatalytic activity. *Ceramics International*, *46*(2), 2421–2437. https://doi.org/10.1016/j.ceramint.2019.09.236

Munawar, T., Mukhtar, F., Yasmeen, S., Naveed-Ur-Rehman, M., Nadeem, M. S., Riaz, M., Mansoor, M., & Iqbal, F. (2021). Sunlight-induced photocatalytic degradation of various dyes and bacterial inactivation using CuO-MgO-ZnO nanocomposite. *Environmental Science and Pollution Research International*, *28*(31), 42243–42260. https://doi.org/10.1007/s11356-021-13572-8

Pachaiappan, R., Rajendran, S., Show, P. L., Manavalan, K., & Naushad, M. (2021). Metal/metal oxide nanocomposites for bactericidal effect: A review. *Chemosphere*, *272*(128607), 128607. https://doi.org/10.1016/j.chemosphere.2020.128607

Pisu, F., Chiriu, D., Ricci, P., & Carbonaro, C. (2020). Defect related emission in calcium hydroxide: The controversial band at 780 cm−1. *Crystals*, *10*(4), 266. https://doi.org/10.3390/cryst10040266

Qi, K., Cheng, B., Yu, J., & Ho, W. (2017). Review on the improvement of the photocatalytic and antibacterial activities of ZnO. *Journal of Alloys and Compounds*, *727*, 792–820. https://doi.org/10.1016/j.jallcom.2017.08.142

Rajabizadeh, A., Abdipour, H., & Mansoorian, H. J. (2025). A new approach for the elimination of Rhodamine B dye using a combination of activated persulfate and dithionite in the presence of magnetic fields. *Genie Des Procedes [Chemical Engineering and Processing]*, *209*(110160), 110160. https://doi.org/10.1016/j.cep.2025.110160

Rani, M., Yadav, J., Shanker, U., & Sillanpää, M. (2023). Green synthesised zinc derived nanocomposites with enhanced photocatalytic activity: An updated review on structural modification, scientific assessment and environmental applications. *Inorganic Chemistry Communications*, *147*(110246), 110246. https://doi.org/10.1016/j.inoche.2022.110246

Rathi, B. S., Kumar, P. S., & Vo, D.-V. N. (2021). Critical review on hazardous pollutants in water environment: Occurrence, monitoring, fate, removal technologies and risk assessment. *The Science of the Total Environment*, *797*(149134), 149134. https://doi.org/10.1016/j.scitotenv.2021.149134

Raveena, & Surendran. (2024). Real-time monitoring and optimisation of recycled water irrigation in coffee plantations using bi-directional RNNs and IoT sensors. *2024 International Conference on Innovation and Intelligence for Informatics, Computing, and Technologies (3ICT)*, 116–123. https://doi.org/10.1109/3ict64318.2024.10824274

Roy, N., Sengupta, R., & Bhowmick, A. K. (2012). Modifications of carbon for polymer composites and nanocomposites. *Progress in Polymer Science*, *37*(6), 781–819. https://doi.org/10.1016/j.progpolymsci.2012.02.002

Salmi, C., Souhaila, M., Salah Eddine, L., Mohammed, H. A. M., Hasan, G. G., & Mahboub, M. S. (2024). Biosynthesis of Mn3O4/PVP nanocomposite for enhanced photocatalytic degradation of organic dyes under sunlight irradiation. *Journal of Cluster Science*, *35*(1), 201–215. https://doi.org/10.1007/s10876-023-02475-y

Salmi, C., Zelca, Z., Laouini, S. E., Meneceur, S., Mohammed, H. A., Abdullah, J. A. A., & Abdullah, M. M. S. (2024). Gallic acid assisted synthesis of novel CuO/Ni/Fe3O4 nanocomposite for catalytic CO2 methanation and photocatalytic hydrogen generation. *Journal of Sol-Gel Science and Technology*. https://doi.org/10.1007/s10971-024-06608-1

Santika, F. T., Suyanto, H., Trisnawati, N. L. P., & Indrayana, I. P. T. (2024). Determination of the optical band gap energy from the extraction and evaporation of anthocyanin compound sea lettuce (Ulva Lactuca L.) using Tauc plot method. *BULETIN FISIKA*, *25*(1), 8. https://doi.org/10.24843/bf.2024.v25.i01.p02

Serouti, A., Eddine, L. S., Meneceur, S., Hasan, G. G., Mohammed, H. A., Salmi, C., Iman, K., Ferhat, M. F., Ali, O. B., & Abdullah, J. A. A. (2024). Biogenic ZnO/CuO/Fe2O3 nanocomposite: A groundbreaking approach for enhanced degradation capabilities and reusability in dye removal applications. *Arabian Journal for Science and Engineering*, *49*(1), 753–764. https://doi.org/10.1007/s13369-023-08495-0

Sharma, R., Giri, S. K., Kumar, A., Chamoli, S., & Singh, G. (2023). ROS-mediated pathogen control by ZnO and MgO nanoparticles. In *Oxides for Medical Applications* (pp. 419–431). Elsevier. https://doi.org/10.1016/b978-0-323-90538-1.00008-x

Shoran, S., Sharma, A., & Chaudhary, S. (2023). Visible light enhanced photocatalytic degradation of organic pollutants with SiO2/g-C3N4 nanocomposite for environmental applications. *Environmental Science and Pollution Research International*, *30*(44), 98732–98746. https://doi.org/10.1007/s11356-022-24837-1

Son, N., Lee, J., Yoon, T., & Kang, M. (2021). Design for a longer photoinduced charge separation and improved visible-light-driven H2 generation through structure reversal and oxygen vacancies via Ni substitution into ZnFe2O4 spinel. *Ceramics International*, *47*(14), 20317–20334. https://doi.org/10.1016/j.ceramint.2021.04.040

Sonocatalyst degradation of catechol from aqueous solution using magnesium oxide nanoparticles. (2023). *Global NEST Journal*, 89–94. https://doi.org/10.30955/gnj.004550

Srinivas, C., Deepty, M., Prasad, S. A. V., Prasad, G., Kumar, E. R., Meena, S. S., Seetala, N. V., Willams, D. D., & Sastry, D. L. (2021). Study of structural, vibrational, elastic and magnetic properties of uniaxial anisotropic Ni-Zn nanoferrites in the context of cation distribution and magnetocrystalline anisotropy. *Journal of Alloys and Compounds*, *873*(159748), 159748. https://doi.org/10.1016/j.jallcom.2021.159748

Subbiah, R., Muthukumaran, S., & Raja, V. (2021). Phyto-assisted synthesis of Mn and mg co-doped ZnO nanostructures using Carica papaya leaf extract for photocatalytic applications. *BioNanoScience*, *11*(4), 1127–1141. https://doi.org/10.1007/s12668-021-00890-x

Subramani, K., Ganeshan, J. K. S., Srinivasan, S., Mohanasundaram, N. V. T., & Incharoensakdi, A. (2025). Hydrothermally and green synthesised TiO2 nanoparticles with high photocatalytic textile industry dye degradation, antibacterial and antioxidant activities. *Journal of Alloys and Compounds*, *1017*(179068), 179068. https://doi.org/10.1016/j.jallcom.2025.179068

Subramani, K., Tamilselvi Mohanasundaram, N. V., Srinivasan, S., Krishnaveni Selva Ganeshan, J., & Incharoensakdi, A. (2025). Microalgae-based bio-fabrication using zinc oxide-chitosan nanocomposite for industrial effluent degradation and pollutant reduction.

International Journal of Biological Macromolecules, *319*(Pt 1), 145379. https://doi.org/10.1016/j.ijbiomac.2025.145379

Tabet, A., Meneceur, S., Laouini, S. E., Salmi, C., Mohammed, H. A., Kir, I., Hasan, G. G., Alharthi, F., & Abdullah, J. A. A. (2024). One post biosynthesis of novel ternary nanocomposite ZnO/CuO/Cu2MgO3 for enhancing photocatalytic degradation of bromocresol green in wastewater. *Journal of Cluster Science*, *35*(3), 765–777. https://doi.org/10.1007/s10876-023-02519-3

Tjardts, T., Elis, M., Hicke, M., Symalla, F., Shondo, J., Drewes, J., Kuru, M., Wolff, N., Faupel, F., Aktas, C., Kienle, L., & Veziroglu, S. (2023). Critical assessment of a TiO2-Ag-ZnO nanocomposite photocatalyst on improved photocatalytic activity under mixed UV-visible light. *Applied Surface Science Advances*, *18*(100500), 100500. https://doi.org/10.1016/j.apsadv.2023.100500

Uddin, F. (2021). Environmental hazard in textile dyeing wastewater from local textile industry. *Cellulose (London, England)*, *28*(17), 10715–10739. https://doi.org/10.1007/s10570-021-04228-4

Vázquez-López, A., Maestre, D., Martínez-Casado, R., Ramírez-Castellanos, J., Píš, I., Nappini, S., & Cremades, A. (2022). Unravelling the role of lithium and nickel doping on the defect structure and phase transition of anatase TiO2 nanoparticles. *Journal of Materials Science*, *57*(14), 7191–7207. https://doi.org/10.1007/s10853-022-07122-x

Venkatraman, & Surendran. (2023, September 20). Aquaponics and smart hydroponics systems water recirculation using machine learning. *2023 4th International Conference on Smart Electronics and Communication (ICOSEC)*. 2023 4th International Conference on Smart Electronics and Communication (ICOSEC), Trichy, India. https://doi.org/10.1109/icosec58147.2023.10276310

Vodyanitskii, Y. N. (2009). Mineralogy and geochemistry of manganese: A review of publications. *Eurasian Soil Science*, *42*(10), 1170–1178. https://doi.org/10.1134/s1064229309100123

Wang, L., Zhang, J., Zhang, Y., Yu, H., Qu, Y., & Yu, J. (2022). Inorganic metal-oxide photocatalyst for H2 O2 production. *Small*, *18*(8), e2104561. https://doi.org/10.1002/smll.202104561

Wastewater recycling integration with IoT sensor vision for real-time monitoring and transforming polluted ponds into clean ponds using HG-RNN. (2025). *Global NEST Journal*. https://doi.org/10.30955/gnj.06758

Wehbi, L., Noun, M., Habanjar, K., & Awad, R. (2023). Investigation of the structural and the physical properties of ZnO–NiO–Mn2O3 nanocomposites for photocatalytic applications. *Applied Physics. A, Materials Science & Processing*, *129*(5). https://doi.org/10.1007/s00339-023-06670-6

Xiao, Z. H., Zhu, Y. Q., Yi, H. T., & Chen, X. Y. (2015). A simple CaCO3-assisted template carbonisation method for producing nitrogen-containing nanoporous carbon spheres and its electrochemical improvement by the nitridation of azodicarbonamide. *Electrochimica Acta*, *155*, 93–102. https://doi.org/10.1016/j.electacta.2014.12.104

Xu, D., Wu, S., Li, Z., Wu, S., Xu, J., & Gu, C. (2025). Aerobic granular sludge treating tannery wastewater and particle size control. *AIP Advances*, *15*(2). https://doi.org/10.1063/5.0255163

Yang, J., Zhang, J., Zhang, J., Zhang, J., Yang, Y., & Zang, L. (2021). Roles of calcium-containing alkali materials on dark fermentation and anaerobic digestion: A systematic review. *International Journal of Hydrogen Energy*, *46*(78), 38645–38662. https://doi.org/10.1016/j.ijhydene.2021.09.129

Zahran, H. Y., Shneouda, S. S., Yahia, I. S., & El-Tantawy, F. (2018). Facile and rapid synthesis of nanoplates Mg(OH)2 and MgO via Microwave technique from metal source:

structural, optical and dielectric properties. *Journal of Sol-Gel Science and Technology*, *86*(1), 104–111. https://doi.org/10.1007/s10971-018-4613-2

Zeghdi, S., Laouini, S. E., Mohammed, H. A., Bouafia, A., Tedjani, M. L., Abdullah, M. M. S., & Trzepieciński, T. (2024). Improved synthesis of Cu2O NPs and ascorbic acid-modified derivatives for adsorption of Brilliant Cresyl Blue: Surface and reusability studies. *Materials*, *17*(10), 2358. https://doi.org/10.3390/ma17102358

Zhu, M., Hu, Y., Li, Y., Jin, H., & Zhu, Z. (2012). Effect of magnetic field on phase morphology transformation of MnO $_2$ nanostructures in a hydrothermal process. *Physica Status Solidi C*, *9*(1), 122–127. https://doi.org/10.1002/pssc.201084200

Zohra, R., Meneceur, S., Eddine, L. S., Bouafia, A., Mohammed, H. A., & Hasan, G. G. (2023). Biosynthesis and characterisation of MnO2 and Zn/Mn2O4 NPs using Ziziphus spina-Christi aqueous leaves extract: Effect of decoration on photodegradation activity against various organic dyes. *Inorganic Chemistry Communications*, *156*(111304), 111304. https://doi.org/10.1016/j.inoche.2023.111304